An epigenetically stabilized regulatory state underlies stable glioblastoma invasion

Ann-Christin Hau

hau@med.uni-frankfurt.de

University Hospital Frankfurt https://orcid.org/0000-0002-4412-2355

Tanja Buhlmann

ta.mueller@med.uni-frankfurt.de

University Hospital Frankfurt https://orcid.org/0000-0001-9521-6186

Sophie Schreiner

Laboratoire National de Santé https://orcid.org/0000-0003-1685-1179

Camille Cialini

Luxembourg Institute of Health https://orcid.org/0009-0007-8688-0983

Vera Laub

University of California, San Francisco https://orcid.org/0000-0002-1301-1118

Petr Nazarov

Luxembourg Institute of Health https://orcid.org/0000-0003-3443-0298

Arnaud Muller

Laboratoire National de Santé https://orcid.org/0000-0002-3841-4722

Kimia Kafi Cheraghi

University Hospital Frankfurt https://orcid.org/0000-0003-4636-0741

Till König

University Hospital Frankfurt

Julia Schwarzpaul

University Hospital Frankfurt

Leander F Harwart

University Hospital Frankfurt

Karl H Plate

University Hospital Frankfurt

Joachim P Steinbach

University Hospital Frankfurt https://orcid.org/0000-0002-4695-2483

Michel Mittelbronn

University of Luxembourg https://orcid.org/0000-0002-2998-052X

Research Article

Keywords: Glioblastoma, invasion, DNA methylation, epigenetic regulation, transcription factor activity, extracellular matrix

Posted Date: September 1st, 2026

DOI: https://doi.org/10.21203/rs.3.rs-10877275/v1

Additional Declarations: The authors declare no competing interests.

Abstract

Glioblastoma is a highly invasive brain tumor in which diffuse infiltration into the surrounding brain parenchyma severely limits therapeutic outcome. While invasion is often described as a plastic and reversible process driven by microenvironmental cues, it remains unclear whether invasive capacity can also be maintained as stable, cell-intrinsic regulatory state. Using a serial *in vitro* selection approach in patient-derived glioma stem-like cultures, we identified a subpopulation with persistently increased invasive potential that was retained under non-selective conditions. Comparative transcriptomic and epigenomic profiling by RNA sequencing and genome-wide DNA methylation analysis using the EPIC array revealed coordinated transcriptional and DNA methylation remodeling associated with the invasive phenotype. Integration of transcription factor activity inference, motif enrichment analysis, and publicly available ChIP-seq chromatin datasets identified convergent invasion-associated regulatory networks and suggested altered accessibility of methylation-sensitive transcription factor binding sites. Representative methylation changes were further recapitulated across an independent panel of patient-derived glioma stem-like cultures individually classified according to their invasive capacity by transwell invasion assays, supporting the broader relevance of the identified epigenetic alterations. Functional perturbation of the transcription factor networks centered on ATF4 and MYC/MAX in established glioblastoma cell lines and patient-derived glioma stem-like cultures demonstrated their contribution to invasive behavior. Finally, invasion-associated transcriptional signatures and a 41-CpG methylation signature significantly stratified overall survival in TCGA IDH-wildtype glioblastoma patients, highlighting the clinical relevance of invasion-associated epigenetic and transcriptional remodeling. Together, these findings support a model that shapes transcription factor activity and maintains invasion-associated gene expression programs.

Introduction

Glioblastoma (GB) is the most aggressive primary brain tumor in adults, characterized by rapid growth, diffuse infiltration, and resistance to current therapies [1], [2], [3]. Among these features, the invasive behavior of GB cells is particularly detrimental, as it precludes complete surgical resection and contributes to inevitable recurrence [4], [5]. Despite the identification of common driver mutations and subtype-specific transcriptional signatures [6], [7], [8], the mechanisms underlying tumor cell infiltration into the surrounding brain parenchyma remain poorly understood. This is in part due to the spatial and functional heterogeneity of GB, comprising distinct subpopulations [9], [10] which results in differential invasive capacity, plasticity, and therapy response. Up to date it remains unclear whether invasion represents a purely dynamic and reversible phenotype or whether stable cell intrinsic invasive states can emerge.

GB invasion is often conceptualized as a transient and reversible phenotype influenced by environmental cues such as growth factors, cytokines, hypoxia or mechanical stimuli [11], [12], [13], [14]. Consistent with this view, marker-defined subpopulations in patient-derived GB stem-like cultures can interconvert and re-establish heterogeneous equilibria over time, supporting intrinsic plasticity that is shaped by the microenvironment [15]. Nevertheless, accumulating evidence suggests that a subset of GB cells may

acquire and maintain stable invasive traits independent of external signals [16], [17]. Such traits could result from clonal selection and be maintained through genetic or epigenetic mechanisms [18], [19] that prime or stabilize invasion-associated regulatory states. Indeed, prior studies have reported that invasive GB cells extracted from *in vivo* models retain their migratory phenotype *ex vivo* [20], [21], [22], [23], [24], implying the existence of cell-intrinsic invasion programs. However, the molecular basis of such stable invasion states, particularly how transcriptional programs may become epigenetically stabilized or maintained, remain largely unexplored.

Invasive behavior in GB has been linked to the activation of gene programs involved in extracellular matrix (ECM) remodeling, cell-matrix interaction, and cytoskeletal dynamics [25], [26]. Spatial transcriptomics and single-cell analyses further suggest that invasive GB cells express neuronal mimicry programs and exhibit enhanced synaptic interaction capacity [27], [28]. The interplay between cancer cells and their surrounding microenvironment has emerged as a critical factor driving the aggressive progression of GB [29], [30]. Many of the key mediators of these interactions are either secreted factors or membrane-bound proteins, enabling them to exert their effects beyond the individual cell, shaping the peritumoral niche and facilitating invasion [31], [32]. Recent multimodal spatial and spatiotemporal studies have further resolved invasion-associated programs and their regional organization, including infiltrative-margin signatures and region-specific matrisome expression in human GB [33], [34], [35]. Although such invasion-associated programs have become increasingly well-defined at the transcriptional level, the mechanisms by which they are maintained or rendered stable remain incompletely understood.

Epigenetic alterations, including changes in DNA methylation and chromatin accessibility, are increasingly recognized as key modulators of cellular identity and plasticity in cancer [36], [37]. Enhancer remodeling and DNA methylation changes in GB have been implicated in the regulation of subtype transitions and therapy resistance [38], [39]. Moreover, DNA methylation may directly influence transcription factor (TF) binding by modifying binding motif accessibility and binding affinity [40], [41], [42], [43], [44]. This raises the possibility that epigenetic reprogramming may contribute to the priming or stabilization of invasion-associated transcriptional programs in GB by selectively enabling or restricting access of TFs to regulatory elements. Here, we established an isogenic serial invasion-selection model that retains a stable invasive phenotype despite prolonged culture in the absence of selection pressure. We show that this phenotype is accompanied by coordinated transcriptional and epigenetic remodeling that converges on invasion-associated TF programs. Differential DNA methylation preferentially affected regulatory elements enriched for the same TF motifs identified by transcriptome-based activity inference and was associated with distinct chromatin states, linking epigenetic remodeling to invasion-associated regulatory networks. These features were further recapitulated across an independent panel of patient-derived glioma stem-like cultures individually classified according to their invasive capacity. Finally, invasion-associated transcriptional and epigenetic signatures, including a 41-CpG methylation signature, were associated with overall survival in TCGA glioblastoma cohorts. Together, our findings support a model in which microenvironmental cues shape may invasion-associated regulatory programs that can become epigenetically stabilized, giving rise to a stable cell-intrinsic invasion-associated regulatory state characterized by coordinated TF activity, DNA methylation remodeling, and chromatin reorganization.

Material and Methods

3D Patient-derived Glioblastoma cell culture

The primary GB cell line BG7 was kindly provided by Prof. Rolf Bjerkvig (University of Bergen, Bergen, Norway). NCH421k and NCH644 cells were purchased from CLS (Eppelheim, Germany). Short tandem repeat (STR) profiling was carried out using Eurofins Genomics services and successfully mapped with public profiles. All glioma stem-like cultures (GSCs) were routinely tested and confirmed to be free of mycoplasma contamination. GSCs were grown as suspension tumor-spheres in NeuroBasal® medium (ThermoFisher #21103049) supplemented with 1% v/v GlutaMAX® (ThermoFisher #35050061), 2% v/v B-27® (ThermoFisher #17504044), 1% v/v Penicillin/Streptomycin (ThermoFisher #15140122), 20 ng/ml animal-free recombinant human epidermal growth factor (EGF, PeproTech #AF-100-15), and 20 ng/ml recombinant human basic fibroblast growth factor (FGF, PeproTech #100-18B) and cultured at 37°C in a humidified atmosphere of 5% CO2. When tumor-spheres reached approximately 300–400 µm in diameter they were dissociated into single cell suspension by incubation with Accutase® (Sigma-Aldrich #A6964) for 10 min at 37°C. Dissociated cells were pelleted, washed once and seeded at 1×105 – 2×105 cells/ml in fresh culture medium.

2D Glioblastoma cell lines and cell culture

The human glioblastoma cell line LN-229 was obtained from the American Type Culture Collection (ATCC). LNT-229 cells (TP53 wild type), which differ from LN-229 only in their TP53 status, were kindly provided by Prof. Michael Ronellenfitsch. LNT-229 cells with stable ATF4 suppression, also kindly provided by Prof. Michael Ronellenfitsch, have been described previously (Lorenz et al., 2021). Cell line authentication was performed prior to experimental use by STR profiling (Multiplexion, Heidelberg, Germany), confirming identity with the published LN-229 STR profile. All cell lines were routinely tested and confirmed to be free of mycoplasma contamination. Cells were cultured at 37°C in a humidified atmosphere containing 5% CO_2 using Dulbecco's Modified Eagle Medium (ThermoFisher #11965092) supplemented with 10% fetal bovine serum (FBS, ThermoFisher #A5256701) and 1% v/v penicillin/streptomycin (ThermoFisher #15140122).

Serial selection for invasive Glioblastoma cells

Serial enrichment of invasive glioblastoma cells was performed using a modified transwell invasion assay, also refer to Fig. 1A. Briefly, Thincert® cell culture inserts (surface area 33.8 mm², pore size 8 µm; Greiner Bio-One #662638) were coated with 25 µg growth factor-reduced Matrigel® basement membrane matrix (Corning #354230) diluted in phosphate buffered saline (PBS) and incubated for at least 2 h at 37°C to allow polymerization. Following removal of excess coating solution, 20,000 cells suspended in culture medium were seeded into each insert. Inserts were transferred into 24 well plates containing culture medium supplemented with 10% FBS in the lower chamber, serving as a chemoattractant, and incubated for 24 h at 37°C. After incubation, non-invading cells remaining on the upper surface of the membrane were carefully removed using pre-wetted cotton swabs. Invaded cells were collected by

combining cells present in the lower chamber medium with cells detached from the underside of the membrane following incubation in 0.25% Trypsin-EDTA (Thermo Fisher Scientific #25200-056) for 5 min at 37°C. Cells recovered from five inserts (corresponding to 100,000 seeded cells) were pooled, washed once, counted, and expanded in fresh culture medium for approximately two weeks. The invasion assay and expansion procedure were repeated for two additional rounds. Cells obtained after the third selection round were designated GB_inv+, whereas the original, unselected parental population was designated GB_naive. To control for potential effects of Matrigel exposure and culture conditions independent of invasion, a parallel control population (GB_ctrl) was generated. GB_ctrl cells were cultured under identical conditions, including Matrigel coating, cell density (20,000 cells), incubation time (24 h), and exposure to 10% FBS. However, cells were cultured directly on Matrigel-coated wells without a transwell membrane and were harvested after 24 h without undergoing invasion.

Transwell invasion assay

Invasive capacity was assessed using Matrigel-coated transwell inserts as described above. Briefly, 20,000 cells were seeded onto Matrigel-coated transwell inserts in serum-free culture medium, whereas the lower chamber contained culture medium supplemented with 10% FBS as a chemoattractant. After 24 h at 37°C, cells were processed according to the respective downstream analysis. For fluorescence-based quantification of GB_naive and GB_inv+ cells, inserts were fixed in 4% paraformaldehyde (Sigma-Aldrich #P6148) for 10 min at room temperature and washed twice with PBS. Non-invading cells remaining on the upper membrane surface were removed using pre-wetted cotton swabs. Membranes were excised using a scalpel, mounted on glass slides using 1.5 µM Fluoromount-G™ containing DAPI (Invitrogen #E36962), and incubated overnight protected from light. Five representative fields per membrane were imaged using a Nikon Eclipse Ni fluorescence microscope (Nikon, Amsterdam, Netherlands) at 10x magnification. Three technical replicates were analyzed for each biological replicate. To assess the migratory capacity of LNT-229 cells with and without stable ATF4 knockdown, as well as LN-229 and BG7 cells following pharmacological inhibition with the MYC/MAX dimerization inhibitor 10058-F4, invaded cells were fixed and stained with 0.5% crystal violet prepared in 10% ethanol. Membranes were washed with PBS, air-dried, and invaded cells were quantified by light microscopy using the EVOSTM M5000 Imaging System (Thermo Fisher Scientific). Five images per membrane were acquired at 20x magnification. Cell quantification was performed using Fiji/ImageJ with a standardized analysis macro. Identical threshold, size, and circularity parameters were applied to all images, and image analysis was performed blinded to the experimental conditions. Each experiment comprised three biological replicates.

Generation of Glioblastoma spheroids

Single-cell suspensions of GB_naive and GB_inv+ cells were prepared and seeded into Nunclon™ Sphera™ 96-well U-bottom plates (Thermo Fisher Scientific #174925) at a density of 1,000 cells per well in 50 µL of glioblastoma stem cell medium. Plates were centrifuged at 300 × g for 3–5 min at 4°C to facilitate cell aggregation and incubated for 24 h at 37°C in a humidified atmosphere containing 5% CO_2 to allow

spheroid formation. Outer wells were filled with PBS and were not used for spheroid generation to minimize edge effects. Following spheroid formation, spheroids were used for subsequent 3D proliferation, adhesion and invasion assays.

3D tumor spheroid invasion assay

The invasive capacity of GB_naive and GB_inv+ spheroids was assessed using a Matrigel-based 3D spheroid invasion assay. Following spheroid formation for 24 h, spheroids were embedded in 100 µL of 1 mg/mL growth factor-reduced Matrigel® diluted in culture medium. Spheroid invasion was monitored by brightfield microscopy using an EVOS M5000 microscope equipped with a monochromatic camera at 10x magnification. Images were acquired after 7, 14, 17, 19, and 21 days of culture. Spheroid core area and invasion area were quantified using Fiji/ImageJ (Schindelin et al. 2012). Twelve technical replicates were analyzed for each condition in four biological replicates.

Cell attachment assay

Cell attachment of GB_naive and GB_inv+ cells was assessed using a crystal violet-based adhesion assay. Flat-bottom 96-well plates (Greiner #655160) were coated with growth factor-reduced Matrigel® (4.5 µL/mm²) diluted in PBS and incubated for at least 2 h at 37°C to allow polymerization. After removal of excess coating solution, 200 viable cells suspended in 100 µL of culture medium were seeded per well and allowed to adhere for 15 min at 37°C in a humidified atmosphere containing 5% CO_2. Non-adherent cells were removed by washing three times with PBS. Attached cells were stained with 0.5% crystal violet for 5 min, washed three times with PBS to remove excess stain, and imaged using an EVOSTM M5000 brightfield microscope equipped with a monochromatic camera at 10x magnification. Four biological replicates with three technical replicates as per each condition were analyzed.

2D proliferation assay

The proliferative capacity of adherent GB_naive and GB_inv+ cells was assessed using a CellCyte X live-cell imaging system (Cytena, Freiburg, Germany). Flat-bottom 96-well plates (Greiner, #655160) were coated with growth factor-reduced Matrigel® (4.5 µL/mm²) diluted in PBS and incubated for at least 2 h at 37°C to allow polymerization. After removal of excess coating solution, cells were seeded at a density of 5×10^4 cells per well in culture medium supplemented with 10% FBS. Brightfield images were acquired every 6 h for 7 days using the CellCyte X (Cytena, Freiburg, Germany) at 10x magnification. The cell-covered area (mm²) was quantified using the integrated CellCyte X image analysis software by applying user-defined masks to brightfield images. Growth curves were generated as fc relative to the first analyzed time point. Three biological replicates with six technical replicates as per condition were analyzed.

3D proliferation assay

To assess spheroid growth, GB_naive and GB_inv+ cells were seeded into Nunclon™ Sphera™ 96-well U-bottom plates at a density of 1,000 cells per well in 100 µL of culture medium. Plates were incubated at 37°C in a humidified atmosphere containing 5% CO_2. Spheroid growth was monitored for 7 days using a CellCyte X live-cell imaging system. Brightfield images were acquired every 6 h at 10x magnification. Spheroid area was quantified using the integrated CellCyte X image analysis software by applying user-defined masks to brightfield images and normalized to day 0, plotted as fold change (fc). Three biological replicates with three technical replicates as per condition were analyzed.

3D dose-response assay and IC $_{50}$ determination

BG7 and U87 spheroids were generated by seeding 10,000 cells in 25 µL culture medium into ultra-low attachment U-bottom 96-well plates (S-Bio #MS-9096UZ) and incubating for 24 h to allow spheroid formation. Uniform spheroid formation was confirmed by brightfield imaging using the CellCyte X Live Cell Analyzer. Spheroids were treated with serial dilutions of the MYC/MAX dimerization inhibitor 10058-F4 (0.1–400 µM) prepared in culture medium containing 500 nM C.LIVE Tox Red (Cytena #D16110024375). Each concentration was tested in triplicates. Control wells received either 0.4% DMSO, 10 µM staurosporine (positive control) or medium alone. After 72 h, cytotoxicity was determined by measuring C.LIVE Tox Red fluorescence using a Varioskan LUX microplate reader (ThermoFisher Scientific). Cell viability was subsequently determined using the CellTiter-Glo® 2.0 assay (Promega #G9241) according to the manufacturer's instructions. Luminescence was recorded using the Varioskan LUX. Fluorescence and luminescence values were normalized to the corresponding control wells, and inhibitor concentrations were log-transformed. Non-linear regression using a log(inhibitor) versus normalized response model was performed in GraphPad Prism (v10.4.1) to calculate IC_{50} values for cytotoxicity and viability.

Flow cytometric analysis of cell death

U87 cells were seeded at 3 × 10^5 cells in 6-cm culture dishes and treated with 0, 15, 30, or 60 µM 10058-F4 for 96 h. Both adherent and detached cells were collected to avoid selective loss of dead cells. Cells were washed with PBS, detached using trypsin, pooled with the corresponding supernatants, and resuspended in FACS buffer (PBS containing 1% FCS). Following centrifugation, cell pellets were resuspended in propidium iodide (PI; 5 µg/mL) and analyzed on a BD FACSCanto™ II flow cytometer. A maximum of 30,000 events per sample was acquired. Cell populations were gated using FlowJo, and PI-positive cells were quantified as a measure of membrane permeability and cell death.

RNA isolation and RT-qPCR

Total RNA was isolated using the RNeasy Mini Kit (Qiagen #74104) according to the manufacturer's instructions, including on-column DNase digestion. RNA concentration and purity were determined by measuring the A260/280 and A260/230 absorbance ratios using the UV-Vis module of the Varioskan. One microgram of total RNA was reverse-transcribed using the RevertAid H Minus First Strand cDNA

Synthesis Kit (Thermo Fisher Scientific #K1621) in a final reaction volume of 20 µL. cDNA was subsequently diluted 1:10 to a final concentration of 5 ng/µL. RT-qPCR was performed using a QuantStudio™ 5 Real-Time PCR System (Thermo Fisher Scientific) with PowerTrack™ SYBR™ Green Master Mix (Thermo Fisher Scientific #A46109). Reactions were performed in technical triplicates in a final volume of 5 µL using primers at a final concentration of 500 nM. Cycling conditions consisted of an initial denaturation at 95°C for 3 min, followed by 32 cycles of 95°C for 10 s and 59°C for 30 s. Melting curve analysis was performed following amplification to confirm primer specificity. Ten genes were selected for validation by RT-qPCR. GAPDH served as the endogenous reference gene. Relative gene expression was calculated using the 2^−ΔΔCt method. Primer sequences are listed below.

Table 1
Primer sequences for RT qPCR

Gene Name	Forward Primer (5´-3´)	Reverse Primer (5´-3´)
PMEPA1	CTGAGCCACTACAAGCTGTCTG	GGATTCCGTTGCCTGACACTGT
MGP	CCTCAGCAGAGATGGAGAGC	GGCAGCATTGTATCCATAAACC
ITGB3	CATGGATTCCAGCAATGTCCTC	TTGAGGCAGGTGGCATTGAAG
IL13RA2	TTGCTTGGCTATCGGATGCT	GGGTTAACTTTTATCTCGGTGTCTGA
cMYC	CCTGGTGCTCCATGAGGAGAC	CAGACTCTGACCTTTTGCCAGG
EPHA3	CTGGCAAGAACCTGAACATC	CTTGAGGCTACTGATGGTAAC
SUSD2	AGAGCTGGATGGACCTGAAA	ATGCCAGCATGATGGAGAC
TNC	TCTCAGGGTCATTCACCACA	CACCGTGCGTGTAATTTCTG
TGFB2	AAGAAGCGTGCTTTGGATGC	GTGCTGAGTGTCTGAACTCC
STX3	CTGGTGGAGAATCAGGGTGAG	TTTCGTTTCATCTCGTGCCTTC
GAPDH	AAATCCCATCACCATCTTCC	TCACACCCATGACGAACA

RNA sequencing

RNA libraries for 8 samples (GB_inv+, N = 4, GB_naive, N = 4) were prepared using the Illumina Stranded mRNA Prep Ligation Kit (polyA selection #20040534), following the manufacturer's protocol. Sequencing was performed on the Illumina NovaSeq platform® (SP200) into two separated flow cells, targeting 19 and 20 million reads per sample (paired-end, 2 × 75 bp). Raw FASTQ files underwent quality assessment using FastQC, FastQ Screen, and RSeQC tools. Preliminary processing included read trimming (Cutadapt (Martin 2011)) and mapping (STAR 2.7.9a (Dobin et al. 2013)) to the human reference genome (GRCh38 – Homo_sapiens.GRCh38.104.gtf). Gene counting, as well as all before mentioned steps, were integrated within a local Snakemake (Mölder et al. 2021) workflow.

Differential gene expression analysis and visualization

Differential gene expression analysis between GB_inv + and GB_naive was performed using the DESeq2 package (v1.32.0) in the R statistical environment. Gene annotation was obtained using the biomaRt package (v2.48.3). Genes with zero variance across samples were excluded prior to normalization. Count data were normalized using the DESeq normalization method and log-transformed. Sequencing-flow-cell batch effects were corrected using ComBat from the sva package for exploratory analyses and visualization. Differential expression analysis was performed using DESeq2 while accounting for sequencing batch. For the final differentially expressed gene (DEG) list, genes with a baseMean < 50 were excluded. DEGs were defined using an adjusted P value (false discovery rate, FDR) < 0.05 and an absolute $\log_2$ fold change ($|\log_2 FC|$) > 1.2. Genes with $\log_2 FC > 1.2$ were considered upregulated, whereas genes with $\log_2 FC < -1.2$ were considered downregulated. Principal component analysis was performed using the DESeq-normalized, log-transformed, and ComBat-corrected expression matrix. Expression values were mean-centered without variance scaling before PCA. For visualization, ellipses representing one standard deviation (1 SD) of biological replicates were added for each experimental group. Heatmaps were generated from the same normalized expression matrix after row-wise Z-score transformation. Hierarchical clustering of genes and/or samples was performed using Euclidean distance and average linkage.

Gene Ontology and pathway enrichment analysis

Functional enrichment analysis was performed using the Database for Annotation, Visualization and Integrated Discovery (DAVID) Bioinformatics Resources v6.8. All differentially expressed genes identified by DESeq2 were submitted as gene symbols using the default human background and default analysis settings. Gene Ontology (GO) enrichment analysis was performed for the Biological Process (BP), Molecular Function (MF), and Cellular Component (CC) categories, and Kyoto Encyclopedia of Genes and Genomes (KEGG) pathway enrichment analysis was performed in parallel. Enrichment significance was assessed using the modified Fisher's exact test (EASE score) implemented in DAVID, and terms with a Benjamini-Hochberg-adjusted p-value < 0.05 were considered significantly enriched. Enrichment results were visualized as bubble plots, with the x-axis representing fold enrichment, bubble size indicating gene count, and bubble color representing the adjusted p-value.

Transcription factor activity analysis using integrated system for motif activity response analysis

To define transcription factor (TF) activity from RNA sequencing data, we used ISMARA (https://ismara.unibas.ch; Balwierz et al. 2014). The gene expression profiles were uploaded on the ISMARA web server to compute TF motif activities based on pre-annotated regulatory regions. ISMARA performed a genome-wide scan to associate differentially expressed genes with known TF binding motifs, estimating TF activity scores in log2(TPM) per transcription factor binding site (TFBS). ISMARA applies internal normalization and statistical modelling to define TF activity, assigning Z-values to indicate the significance of each TF’s regulatory impact. No fixed Z-value cut-off was applied by ISMARA. Following

the analysis, activity tables were downloaded from ISMARA for both unaveraged and averaged sample datasets. To identify the top transcription factors with differential activity, the averaged dataset was sorted by Z-value (activity significance, the range of Z-values for selected transcription factors spanned from 7.34 to 2.91) and top 50 transcription factors were selected for visualization. The corresponding activity scores from individual samples for these TFs were then retrieved from the unaveraged dataset. For visualization, we generated a heatmap using GraphPad Prism, applying the color scale feature to represent transcription factor activity levels across samples. To facilitate clustering and pattern recognition, TFs were sorted based on their activity differences between invasive and non-invasive cells, ranking them from high to low activity in invasive cells relative to non-invasive cells.

DNA methylation assay

Genomic DNA was extracted using the DNeasy Blood & Tissue Kits (Qiagen #69504) according to the manufacturer`s instructions. DNA was eluted in 50 µL nuclease-free water, and DNA concentration was determined using a Qubit™ 3 Fluorometer (Invitrogen). Genome-wide DNA methylation profiles were generated using the Infinium MethylationEPIC BeadChip® (Illumina) according to the manufacturer's instructions. Raw methylation data (IDAT files) were processed using the RnBeads package (Assenov et al. 2014) in R. Quality control included removal of probes failing the detection p-value threshold, probes overlapping known single nucleotide polymorphisms (SNPs), cross-reactive probes, and probes located on the sex chromosomes. Beta values were normalized using the BMIQ normalization method implemented in RnBeads.

Differentially methylated probes (DMP) analysis

Delta beta (Δβ) value is defined as the average beta value of GB_inv+ samples minus the average beta value of GB_naive samples. $\Delta\beta \geq 0.2$ or ≤ -0.2 with FDR < 0.05 were considered differentially methylated. According to that criteria there were 7288 differentially methylated probes (DMP) when comparing GB_inv + vs GB_naive (4332 hyper-methylated probes and 2956 hypo-methylated probes). Only probes that could be annotated to a gene were further considered. Probes annotated to lncRNAs or miRNAs were excluded, as well as probes annotated to uncharacterized homologues (LOC). After exclusion 4234 differential methylated genes (DMGs) could be identified, 1278 hyper-methylated and 1294 hypo-methylated gene probes.

Copy number variation (CNV) analysis

Copy number variation (CNV) profiles were inferred from Infinium MethylationEPIC BeadChip data using the Epignostix analysis platform (Heidelberg, Germany, https://epignostix.com/). Raw IDAT files were uploaded to the platform, which generated gene-level CNV segment files containing genomic coordinates, gene annotations, segment $\log_2$ ratios, and probe counts for each sample. These segment tables were exported as tab-delimited text files and used for downstream analyses in Python. Chromosome-level CNV profiles were generated by calculating the probe number-weighted mean segment $\log_2$ ratio for each chromosome. Pairwise similarity between samples was assessed using Pearson correlation coefficients calculated from the chromosome-level CNV profiles and visualized as a correlation heatmap. Gene-level

CNV plots were generated from the exported segment files using the genomic coordinates and corresponding segment $\log_2$ ratios. Three biological replicates per condition were analyzed.

Integrated epigenomic and transcription factor analyses

Transcription factor motif retrieval

TF binding motifs were obtained from the JASPAR 2024 database (https://jaspar.genereg.net), an open-access repository of manually curated and experimentally validated TF binding profiles (Rauluseviciute et al. 2024). Motifs were downloaded as position weight matrices (PWMs) and used for visualization and comparison of candidate transcription factor binding motifs identified in downstream analyses.

Central motif enrichment analysis

Central motif enrichment analysis was performed using CentriMo from the MEME Suite (v5.5.1) with default parameters (Bailey et al. 2012). DNA sequences spanning ± 200 bp around significantly differentially methylated CpG sites were extracted from the hg19 human reference genome. Hypermethylated and hypomethylated CpG sites identified in GB_inv+ compared with GB_naive cells were analysed separately. Motif enrichment was assessed against the HOCOMOCO v12 CORE human transcription factor motif database. Statistical significance was evaluated using CentriMo E-values, Fisher E-values, and Benjamini–Hochberg-adjusted p-values as implemented in the CentriMo workflow. Motif enrichment plots were generated directly from the CentriMo output.

Integration of public epigenomic datasets

To investigate the chromatin context of differentially methylated regions, EPIC-derived CpG sites were classified according to their methylation status using a custom Python 3 script available at https://github.com/veritasnondatur/sequencing_file_workup/blob/main/coordinate_extension_final.ipynb. CpG sites with $\Delta\beta \geq 0.2$ were classified as hypermethylated, whereas sites with $\Delta\beta \leq -0.2$ were classified as hypomethylated. For integrative chromatin analyses, genomic coordinates were extended by ± 1000 bp to capture the surrounding regulatory landscape. Publicly available ChIP-seq and whole-genome bisulfite sequencing datasets generated in U87 glioblastoma cells were retrieved from ChIP-Atlas. ChIP-seq datasets were mapped to the hg19 reference genome and filtered using a significance threshold of $q < 1 \times 10^{-5}$. The selected datasets comprised H3K27ac (SRX129073), H3K4me3 (SRX129079), MED1 (SRX129090), MAX (SRX129085), MYC (SRX129069), and E2F1 (SRX2841182). Corresponding whole-genome bisulfite sequencing data (SRX381701) were analyzed in parallel. Original CpG coordinates as well as the ± 1000 bp extended regions were analyzed using ChAse (v1.1.2) to determine overlap with public ChIP-seq peaks. Signal intensity values were subjected to k-means clustering (k = 2) and visualized as heatmaps to identify relationships between DNA methylation, chromatin activation, and transcription factor occupancy.

Integrative genomic visualization

Representative loci were visualized using the Integrative Genomics Viewer (IGV) (v2.18.2). Original (non-extended) differentially methylated CpG sites were displayed together with public U87 ChIP-seq tracks for

H3K27ac, H3K4me3, MYC, and MAX, as well as corresponding bisulfite sequencing data. Candidate loci (TNC, FLNC, and TGFB2) were selected based on differential gene expression and DNA methylation between GB_inv + and GB_naive subpopulations. This integrative visualization enabled the direct comparison of DNA methylation status with chromatin activation marks and transcription factor occupancy at representative invasion-associated loci.

Survival analysis and prognostic risk score generation

Overall survival (OS) analyses were performed using publicly available The Cancer Genome Atlas (TCGA) IDH wild-type glioblastoma datasets comprising RNA sequencing and DNA methylation data. TCGA data were downloaded using the RTCGA package (v1.6.0) in R (v3.4.2). RNA sequencing data consisted of Level 3 RSEM-normalized gene expression values, which were $\log_2$-transformed prior to Cox regression analysis. To construct an RNA expression-based prognostic signature, the differentially expressed genes identified between GB_inv + and GB_naive cells were evaluated by univariate Cox proportional hazards regression in 240 IDH wild-type glioblastoma patients. P-values were adjusted for multiple testing using the Benjamini–Hochberg procedure, and genes with an FDR < 0.01 were retained for signature construction, resulting in a 79-gene prognostic signature. For each patient, a gene-based risk score was calculated as the weighted sum of $\log_2$-transformed RSEM-normalized expression values using the corresponding Cox regression coefficients as weights.

DNA methylation data deposited in TCGA were generated using the Illumina HumanMethylation450 BeadChip. Owing to differences in probe coverage between the HumanMethylation450 and Infinium MethylationEPIC arrays, only CpG sites represented on both platforms were considered for downstream analyses. For methylation-based analyses, differentially methylated CpG sites identified in the present study were analysed using the same workflow in 147 IDH wild-type glioblastoma patients. CpG sites significantly associated with overall survival (FDR < 0.05) were retained, resulting in a 41-CpG prognostic signature. Methylation-based risk scores were calculated analogously using the corresponding Cox regression coefficients as weights.

Patients were stratified into high-risk and low-risk groups according to the median risk score, and survival differences were assessed using Kaplan–Meier survival analysis, log-rank tests, and Cox proportional hazards regression. A combined prognostic score was generated by z-score normalization of the gene expression- and methylation-derived risk scores followed by summation of both standardized scores. The combined score was subsequently dichotomized using the median value for survival analysis. Survival analyses and risk score calculations were performed in R (v4.4.2) using the survival package. Kaplan–Meier survival analyses of individual CpG sites were performed using the MethSurv platform (Modhukur et al. 2018) based on the TCGA Glioblastoma (2017) cohort using the default analysis settings.

Statistical analysis

Statistical analyses of functional experiments were performed using GraphPad Prism (v10.4.1; GraphPad Software, Boston, USA). Comparisons between two groups were performed using unpaired two-tailed Student's t-tests, applying Welch's correction where appropriate. Comparisons involving more than two

groups were analysed using ordinary one-way analysis of variance (ANOVA) followed by Tukey's multiple-comparison test. Data are presented as mean ± SEM from at least three independent biological experiments unless otherwise stated. P-values < 0.05 were considered statistically significant (shown as *p < 0.05, **p < 0.01, ***p < 0.001, and ****p < 0.0001). Statistical analyses for RNA sequencing, DNA methylation, transcription factor motif enrichment, functional enrichment, copy number variation, and survival analyses were performed using the statistical methods implemented in the respective software packages as described in the corresponding Methods sections.

Results

Invasive glioblastoma cells display a stable invasive phenotype

To interrogate whether invasive capacity can also be maintained as a cell-intrinsic program and stably selected, we isolated a highly invasive subpopulation (GB_inv+) from an isogenic parental population (GB_naive) (Fig. 1A) using serial transwell-based selection in patient-derived GB stem-like cultures (GSCs). To control for potential confounders, including extracellular matrix exposure, chemoattractant conditions, and handling, we generated a matched control population (GB_ctrl) that was processed in parallel under identical conditions but was not required to migrate through a transwell membrane, where cells were recovered after incubation without invasion selection. Quantification of invasion revealed an approximately tenfold increase in GB_inv+ relative to GB_naive, whereas GB_ctrl showed only a modest increase compared with GB_naive (Fig. 1B-C). These findings indicate that GB_inv+ cells retain their phenotype even in the absence of continuous selection pressure, suggesting that selection of a stable cell-intrinsic state, potentially supported by genetic or epigenetic alterations, underlies the persistent invasive phenotype.

To validate these findings, we next performed a 3D tumor spheroid invasion assay (Fig. 1D-E). Increased invasion of GB_inv+ cells was detectable 17 d after embedding and remained stable throughout the experiment. The invasive phenotype persisted across subsequent culture and freeze-thaw cycles, consistent with previous observations that invasive behavior can be retained *ex vivo* [45]. Importantly, enrichment of the invasive phenotype was reproducibly observed across four independently generated GB_inv+ populations, supporting the robustness of the selection approach. Moreover, the phenotype remained stable for more than 10 passages in the absence of further selection pressure, arguing against a purely transient adaptive response.

In contrast, GB_inv+ cells did not display a proliferative advantage. Instead, both 3D spheroid growth and 2D proliferative expansion were significantly reduced in GB_inv+ cells compared with GB_naive cells (Fig. 1F-G; Supplementary Fig. S1A), indicating that enhanced invasion is not accompanied by increased proliferative capacity. Adhesion properties were not significantly altered (Supplementary Fig. S1B). Morphologically, GB_inv+ cells exhibited a more elongated, mesenchymal-like appearance characterized by increased front–rear polarity and protrusive structures (Supplementary Fig. S1C), consistent with their

invasive phenotype. Together, these results demonstrate that serial invasion selection enriches a GB_inv+ subpopulation with a stable invasive phenotype that persists under standard culture conditions and is accompanied by altered cellular morphology and reduced proliferative expansion. The phenotype cannot be explained by enhanced growth, adhesion differences, or gross CNV divergence (Fig. 1H-I; Supplementary Fig. S2). These findings are consistent with a model in which invasive capacity can be stably maintained as a cell-intrinsic state.

Invasive glioblastoma cells exhibit a distinct invasion-associated transcriptional program

To characterize the transcriptional changes associated with the stable invasive phenotype, we performed comparative bulk RNA sequencing (GB_inv + vs GB_naive, n = 4 biological replicates; Fig. 2A). Principal component analysis (PCA) based on the global expression dataset revealed a clear separation between the two populations, with samples clustering according to condition, indicating a robust and reproducible transcriptional divergence associated with invasiveness (Fig. 2B). Differential expression analysis was performed on protein-coding transcripts (baseMean ≥ 50) using a threshold of |log2(fold change)| ≥ 1.2 and FDR < 0.05. This analysis identified 636 differentially expressed genes (DEGs), including 366 upregulated and 270 downregulated genes in GB_inv+ compared with the isogenic GB_naive population (Fig. 2C, Supplementary Fig. 3A). To provide a biologically guided overview of the invasion-associated transcriptional program, selected differentially expressed genes were grouped according to their functional annotation. The resulting heatmap demonstrates coordinated regulation of genes involved in extracellular matrix remodeling, cell adhesion, migration, cytoskeletal organization, cell cycle regulation and signalling pathways that collectively characterize the invasive phenotype (Fig. 2D). An unsupervised heatmap of the top100 differentially expressed genes is shown in Supplementary Figure S3C.

Gene Ontology (GO) analysis of biological processes on the combined set of DEGs revealed overrepresentation of terms related to cell migration and motility, extracellular matrix organization, secretion and export, cell projection organization, and signal transduction, and neuronal projection-associated processes, suggesting broader remodeling of cell–environment interaction programs in invasive cells (Fig. 2E). Consistently, pathway analysis highlighted focal adhesion, ECM-receptor interaction, PI3K-AKT, MAPK, and WNT signaling (Fig. 2F). Cellular component and molecular function analyses further indicated enrichment of extracellular region, plasma membrane, anchoring junction, transport vesicle, and receptor-associated binding activities (Supplementary Fig. S3D-E).

Finally, RNA sequencing results were validated by RT-qPCR using independent cDNA preparations. Expression changes of selected invasion-associated genes showed strong agreement with the RNA-seq dataset (adjusted $R^2 = 0.8194$), confirming the robustness of the identified transcriptional alterations (Fig. 2G; Supplementary Figure S3B; Table 1).

Together, these findings indicate that invasive GB cells engage a coordinated transcriptional program linked to cell motility, extracellular remodeling, and cell-environment signaling. Importantly, this program

persists independently of external invasion cues.

Distinct transcription factor activity underlies invasion-associated transcriptional remodeling

To identify upstream regulatory programs associated with the stable invasive state, we inferred transcription factor (TF) activity from the RNA-seq data using the Integrated System for Motif Activity Response Analysis (ISMARA). A schematic overview of the analysis workflow is shown in Fig. 3A. ISMARA estimates transcription factor activity based on coordinated changes in the expression of predicted target genes rather than transcription factor expression itself, thereby enabling the identification of regulatory programs underlying the invasion-associated transcriptional state. Across 603 analyzed motifs, 101 (16.74%) showed significantly altered activity between GB_inv + and GB_naive cells at a threshold of $|Z| \geq 2$, including 61 motifs with $|Z| \geq 2.58$ and 49 motifs with $|Z| \geq 3.0$ (Fig. 3B). Heatmap visualization of the top differentially active motifs revealed a clear and consistent shift in TF motif activity between GB_inv + and GB_naive cells (Fig. 3C). Among the top-ranking motifs with increased activity in GB_inv+ cells were SOX, FOX, ATF4, CEBPB, SP1, TCF12/ASCL2 families, whereas motifs with higher activity in GB_naive were dominated by E2F family members, MYC-associated motifs, TFDP1, and NFY-related factors (Fig. 3C, E). Because DNA methylation can directly interfere with TF binding when CpG dinucleotides are present within their recognition sequences, we next assessed the CpG content of the consensus binding motifs corresponding to the differentially active TF families. Approximately 67% of the top differentially active motifs with biologically meaningful downstream pathway associations contained one or more CpG dinucleotides within their consensus binding sequences, suggesting that a substantial proportion of the identified regulatory programs may be susceptible to methylation-dependent modulation (Fig. 3D). Representative consensus motifs are shown in Fig. 3E.

Importantly, these changes in inferred TF activity were not paralleled by corresponding changes in TF gene expression. Only a subset of motif-associated TFs showed altered expression between GB_inv + and GB_naive cells, with HSF4 representing the only upregulated factor exceeding the applied RNA-seq significance threshold (Supplementary Fig. S4A). However, HSF4 did not belong to the most strongly differentially active motifs ($Z \geq 3$), underscoring that altered TF abundance alone does not explain the observed regulatory differences.

To functionally interpret the inferred changes in TF activity, pathway enrichment analysis was performed on the predicted target gene sets contributing to the activity shift of each differentially active TF motif (Supplementary Fig. S4B). Downstream pathway analysis of gene sets associated with differentially expressed TFs, including HSF4, GATA2, and GFI1B, yielded only sparse or heterogeneous enrichments and therefore did not provide a comparably coherent framework for interpretation. On the other hand, motifs with predicted higher activity in GB_inv+ cells mapped predominantly to extracellular matrix regulation, adhesion- and migration-associated programs, and broader signaling-state pathways. Within this group, ATF4 and CEBPB were most strongly linked to extracellular matrix regulation, whereas TCF12/ASCL2, SOX, and SP1 were linked more directly to adhesion- and migration-related programs. FOX-associated pathways pointed to broader developmental and signaling-state pathways involving Wnt/β-catenin, p53,

and adherens junction signaling, while MLX-associated motifs were linked to Wnt, mTOR, PI3K, cytokine, and E-cadherin-related signaling. Motifs with lower activity in GB_inv+ cells were predominantly enriched for cell cycle-associated regulators, particularly E2F family motifs (Supplementary Fig. S4B).

However, several motif groups showed more complex or intermediate downstream associations. NFY-related factors were more strongly linked to secreted and extracellular target programs, whereas TFDP1 and MYC-associated motifs occupied an intermediate position, combining cell cycle-associated features with adhesion-, ECM-, and signaling-related pathways. These patterns indicate that, rather than forming strictly discrete modules, transcriptional programs associated with proliferation and extracellular interaction partially overlap at the regulatory level. Together, these findings demonstrate that the invasion-associated transcriptional state is characterized by coordinated changes in TF activity that are largely independent of TF expression. The high prevalence of CpG-containing consensus motifs among the most strongly differentially active TF families provides a mechanistic link between altered TF activity and DNA methylation, thereby establishing the rationale for the subsequent epigenetic analyses.

Invasive glioblastoma cells exhibit targeted DNA methylation remodeling at regulatory elements

Encouraged by the pronounced activity shift of several top differentially active TF motifs containing CpG dinucleotides within their recognition sequences, we next investigated whether the invasion-associated regulatory state was accompanied by global epigenetic remodeling. Genome-wide DNA methylation profiling was performed using the Infinium MethylationEPIC 850K array (Fig. 4A). Although this platform does not provide complete methylome coverage, it is enriched for CpG loci associated with regulatory elements relevant to cancer biology. While not specifically designed for glioma, it has proven useful for detecting glioma-relevant epigenetic alterations [46]. PCA revealed a clear separation between the isogenic GB_inv + and GB_naive samples, indicating consistent differences in global methylation patterns associated with the invasive state (Fig. 4C). Applying an FDR threshold < 0.05 followed by a Δβ cutoff of ≥ 0.2 identified 7,288 differentially methylated probes (DMPs), comprising both hypermethylated (4,332 DMPs) and hypomethylated (2,956) sites in GB_inv+ cells (Fig. 4B, D). Genomic annotation revealed distinct distributions of hyper- and hypomethylated loci. Hypermethylated probes were relatively enriched at promoter-proximal, first-exon and CpG island-associated regions, whereas hypomethylated probes were more frequently observed in gene body-associated contexts (Fig. 4E-G). Extending the analysis to enhancer-associated regions demonstrated a relative enrichment of hypomethylated loci within enhancer elements, particularly FANTOM5-annotated enhancers, supporting widespread remodeling of distal regulatory elements beyond promoter-associated methylation (Supplementary Fig. S4E). While promoter methylation is generally more closely associated with transcriptional repression, gene body and enhancer methylation are considered more context dependent. The predominance of hypomethylation within these regulatory compartments therefore suggests broad epigenetic remodeling rather than a purely promoter-driven mechanism.

At the gene level, hypermethylated loci mapped to 1,278 unique annotated genes and hypomethylated loci to 1,294 unique annotated genes. Because individual genes frequently contained multiple DMPs and

could simultaneously harbor promoter- and gene body-associated methylation changes, gene lists were de-duplicated within each annotation category. Genes containing both hyper- and hypomethylated regions (n = 116) were excluded from downstream enrichment analyses to avoid ambiguous functional assignment.

Gene ontology analysis demonstrated that hypomethylated genes shared between promoter and gene body regions were predominantly enriched for biological processes associated with cell migration, locomotion, actin cytoskeleton organization and cell-matrix adhesion (Fig. 4H). Complementary Cellular Component analysis confirmed enrichment of focal adhesions, cell-substrate junctions and leading-edge structures (Supplementary Fig. S4C). Gene body-associated hypomethylated genes displayed a broader functional profile, including cytoskeletal organization, cell junction assembly, morphogenesis and intracellular signalling (Fig. 4I), accompanied by enrichment of cytoskeletal and junction-associated cellular compartments (Supplementary Fig. S4D). Together, these findings indicate that gene body hypomethylation contributes to extensive structural remodeling beyond the more focused migration-associated program observed for genes affected in both promoter and gene body regions. Hypermethylated gene sets, rather than converging on migration-associated functions, were preferentially enriched for neuronal, synaptic, and cell–cell communication-related terms, including synaptic signaling, neuron projection-associated structures, and junctional components.

These findings suggest not a general reduction in microenvironmental interaction but a qualitative shift from neuronal or synapse-associated programs toward a more dynamic, matrix- and motility-oriented invasive state. Consistently, DNA methylation changes in invasive glioblastoma cells follow a directional, context-dependent pattern, with hypomethylation linked to cytoskeletal and cell–matrix programs and hypermethylation associated with repression of alternative cellular programs.

DNA methylation remodeling identifies functionally relevant transcription factor networks underlying glioblastoma invasion

To further investigate the regulatory consequences of the invasion-associated DNA methylation changes, we examined whether differentially methylated CpG sites were preferentially enriched within TF binding motifs using CentriMo, which identifies positional enrichment of known TF binding motifs around a set of genomic regions.

CentriMo analysis revealed that hypomethylated CpG sites in GB_inv+ cells were significantly enriched for motifs recognized by members of the CREB/ATF family, including CREB3L4 and GMEB2, as well as MLX-related bHLH transcription factors (Fig. 5A). Because DNA methylation within CpG-containing recognition sequences can interfere with transcription factor binding, hypomethylation at these loci is consistent with increased accessibility of regulatory elements associated with stress response and metabolic adaptation programs linked to the invasive phenotype. In contrast, hypermethylated CpG sites showed strong enrichment for E-box-containing motifs (CACGTG), which are recognized by basic helix–loop–helix (bHLH) TFs, including members of the MYC/MAX/MNT network (Fig. 5B). Among these, MNT-associated

motifs exhibited the highest statistical significance, followed by MYC and MAX. Additional enrichment of HIF/ARNT-related motifs was also observed. Hypermethylation at these CpG-containing binding motifs is therefore consistent with reduced accessibility of canonical bHLH regulatory elements, suggesting selective epigenetic remodeling of distinct transcription factor networks rather than random redistribution of DNA methylation across the genome.

To place these motif-level observations into a chromatin context, we integrated publicly available epigenomic datasets from U87 glioblastoma cells, a widely used *in vitro* model with high invasive capacity in our transwell assay. This included ChIP-seq profiles for active histone marks (H3K27ac, H3K4me3), the mediator complex subunit MED1, and TFs MAX, MYC, and E2F1, as well as bisulfite sequencing data. Hypomethylated CpG-centered regions displayed strong enrichment for H3K27ac, H3K4me3 and MED1, accompanied by focal MYC/MAX occupancy, whereas hypermethylated regions exhibited weaker chromatin activation signals and reduced TF binding (Fig. 5C-D; left). These differences remained evident when surrounding ± 1 kb regions were analyzed and were further reflected in average chromatin signal profiles (Fig. 5C-D; right; Supplementary Fig. S5E). Representative loci illustrated the concordance between DNA methylation, chromatin state and transcription factor occupancy, with hypomethylated TGFB2 and TNC loci exhibiting active chromatin features and MYC/MAX binding, whereas the hypermethylated FLNC locus showed comparatively weaker occupancy (Supplementary Fig. S5A-C). Importantly, methylation patterns at these loci consistently correlated with invasive behavior across an independent panel of patient-derived glioma stem-like cultures that had been individually classified according to their invasive capacity using transwell invasion assays, indicating that these epigenetic alterations are not restricted to the serial invasion-selection model but are also observed in biologically distinct glioblastoma models (Supplementary Fig. S5D).

To determine whether the identified regulatory programs contribute functionally to glioblastoma invasion, we selected representative transcription factor networks from both directions of the inferred activity spectrum. Because no direct pharmacological ATF4 inhibitor is available, we used genetic ATF4 knockdown, whereas MYC-dependent transcriptional activity was addressed pharmacologically using the MYC/MAX dimerization inhibitor 10058-F4.

Knockdown of ATF4 in LNT-229 cells resulted in a significant reduction in invasive capacity compared to non-targeting controls (Fig. 5E), supporting a functional contribution of ATF4-associated transcriptional programs to invasion-related phenotypes. The ATF4 knockdown model was previously established and characterized (Lorenz et al., 2021), demonstrating efficient target suppression without inducing major cytotoxic effects under baseline conditions. Consistent with this, the reduced invasion observed here is unlikely to reflect general loss of viability, but rather a more specific role of ATF4-dependent regulatory programs in promoting invasive behavior.

Likewise, pharmacological disruption of MYC/MAX dimerization using 10058-F4 significantly impaired invasion in both adherent LN-229 cells and patient-derived glioma stem-like cells following 72 h pretreatment (Fig. 5F-G). Dose-response and flow cytometric analyses established that concentrations up to 30 µM did not induce substantial cytotoxicity, thereby defining a non-toxic concentration range for

invasion assays (Supplementary Fig. S6A-E). Together, these findings demonstrate that invasion-associated DNA methylation remodeling converges on functionally relevant TF networks, linking altered methylation at regulatory elements with chromatin organization and TF programs that directly contribute to glioblastoma invasion. This supports a model in which the invasive phenotype reflects an intrinsically primed regulatory state, rather than being driven by a single dominant factor, and emerges from the coordinated interplay of distinct and context-dependent transcriptional activities.

Clinical relevance of invasion-associated epigenetic and transcriptional signatures

To assess the clinical relevance of invasion-associated transcriptional and epigenetic alterations, we derived methylation- and gene expression-based risk scores using Cox proportional hazards modeling in TCGA IDH-wildtype glioblastoma patients. The final methylation- and gene-based signatures comprised 41 CpG sites (n = 147 patients) and 79 genes (n = 240 patients), respectively. Both scores significantly stratified patient survival, with the methylation-based model showing particularly strong prognostic power. Importantly, combining both signatures did not substantially improve prediction beyond the methylation-based model alone, highlighting the strong prognostic value of the invasion-associated methylation program (Fig. 6A-C).

Consistent with these findings, invasion-associated CpG methylation patterns identified *in vitro* were preserved across patient samples, as demonstrated by clustering analyses (Fig. 6D-E). Representative hypomethylated CpG sites from the invasion-associated methylation signature (NPFFR1, ITGA2, CD44 and DCLK1) were each significantly associated with reduced overall survival in independent patient cohorts using the MethSurv platform (Fig. 6F-I). While individual CpG sites could not be uniformly evaluated across datasets due to differences in probe coverage between EPIC and 450k arrays, the overall consistency supports the clinical relevance of invasion-associated epigenetic alterations.

Complementary transcriptomic analyses yielded similar findings. The invasion-associated gene expression signature clearly separated GB_naive and GB_inv+ cells and remained preserved across TCGA IDH-wildtype glioblastoma samples (Supplementary Fig. S7A-B). Furthermore, representative genes from this signature, including ICAM1, LSP1, and COL22A1, were each significantly associated with patient outcome in an independent cohort using GEPIA2 (Supplementary Fig. S7C), supporting the clinical relevance of the identified invasion-associated transcriptional program.

Together, these findings demonstrate that the invasion-associated epigenetic and transcriptional signatures identified in our experimental model are retained in human glioblastoma and capture clinically relevant regulatory states associated with patient outcome. The particularly strong performance of the methylation-based signature further suggests that invasion-associated DNA methylation remodeling represents a robust biomarker of aggressive glioblastoma biology.

Discussion

Invasion into the surrounding brain parenchyma is a defining feature of glioblastoma and a major obstacle to effective therapy. While glioblastoma invasion is often described as a plastic and reversible process driven by microenvironmental cues, our data support an alternative, complementary model in which invasion can be partially maintained as a stable, cell-intrinsic state. Using serial transwell selection in patient-derived glioma stem-like cells, we isolated an invasive subpopulation that retained its phenotype across long-term culture without invasion selection pressure. This state was accompanied by a distinct transcriptional program, targeted DNA methylation changes at regulatory elements, and altered TF activity, supporting a model in which invasion is associated with an epigenetically primed regulatory state that persists under non-selective conditions.

The prevailing view of glioblastoma invasion emphasizes dynamic and reversible cellular behavior shaped by external signals such as growth factors, cytokines, and mechanical cues [11], [29], [47], [48], [49]. While this dynamic regulation is well established, our data indicates that a subset of glioblastoma cells can maintain invasive capacity independently of continuous external input. The absence of major differences in proliferation or adhesion between GB_inv + and GB_naive cells argues against a general fitness advantage and instead supports the existence of a specific and heritable invasion program. This is consistent with previous studies showing that invasive glioblastoma cells can retain their migratory phenotype ex vivo, independent of niche-derived signals [20], [48], [50], [51], [52]. Together, these findings suggest that glioblastoma invasion is best understood as a combination of dynamic plasticity and stable, cell-intrinsic states.

At the transcriptional level, this stable invasive state was associated with a coordinated program enriched for extracellular matrix remodeling, adhesion, and signaling pathways such as PI3K–AKT and MAPK, all of which are established contributors to glioblastoma cell motility and invasiveness [53], [54]. These patterns indicate the activation of a transcriptional network supporting cytoskeletal remodeling, cell–matrix interaction, and adaptive signaling. Consistent with recent single-cell and spatial transcriptomic studies, glioblastoma comprises distinct, yet plastic, cellular states characterized by differential interaction with the extracellular matrix and adaptive transcriptional programs [8], [28], [55]. However, chromatin-based analyses have further shown that these cellular states are embedded within defined regulatory landscapes, suggesting that transcriptional programs are constrained by underlying epigenetic configurations rather than representing purely transient responses [56].

Our epigenomic analyses suggest that this regulatory framework is shaped, in part, by context-dependent DNA methylation changes at regulatory elements. Rather than exhibiting a strong global correlation with gene expression, invasion-associated DNA methylation changes were preferentially localized to promoter-proximal and enhancer-associated regulatory elements and were associated with distinct chromatin states and transcription factor (TF) binding patterns. Although chromatin profiling relied on publicly available datasets from U87 glioblastoma cells and therefore provides supportive rather than direct evidence within our experimental system, the convergence of DNA methylation remodeling, TF activity inference, and chromatin annotations suggests coordinated epigenetic remodeling at invasion-associated regulatory elements. While our data do not demonstrate that DNA methylation directly alters TF

occupancy, they support a model in which hypomethylation facilitates TF engagement at invasion-associated loci, whereas hypermethylation may reduce accessibility at canonical binding sites, including E-box-containing regions associated with the MYC/MAX/MNT network.

Together, these data reveal convergence between DNA methylation remodeling and transcription factor-associated regulatory networks in the context of glioblastoma invasion and suggest that methylation-sensitive transcriptional regulators may act as key effectors of the invasive state [44], [57], [58], [59]. More broadly, this concept aligns with emerging evidence that DNA methylation contributes to the stabilization of regulatory states by shaping chromatin landscapes rather than directly dictating gene expression [60], [61]

In line with this model, transcription factor activity was markedly shifted in invasive cells without corresponding changes in TF expression. Stress-responsive regulators, including ATF4, were increased, whereas transcriptional programs commonly associated with cell cycle regulation, including MYC-related signatures, were reduced at the activity level. These findings are consistent with a reconfiguration of transcription factor activity within an altered epigenetic landscape rather than simple up- or downregulation. MYC-dependent regulation does not appear to be globally suppressed but rather redistributed toward a distinct set of regulatory elements, rather than uniformly reduced. This is supported by our observation that pharmacological inhibition of MYC/MAX dimerization impairs invasion without inducing cytotoxicity, indicating that MYC/MAX-dependent transcriptional activity contributes to invasion-associated cellular behavior. Previous studies similarly highlight context-dependent roles of MYC beyond proliferation-associated programs [62], [63]. In parallel, increased ATF4 activity and the reduction of invasion upon ATF4 knockdown support a functional role of ATF4-associated transcriptional programs in invasive behavior [64]. While ATF4 emerged as a top-ranked regulator at the level of inferred activity and functional perturbation, chromatin-level analyses were primarily feasible for MYC/MAX due to the availability of high-resolution public datasets. Future studies will need to define the chromatin context of ATF4-dependent regulation in invasive glioblastoma.

Taken together, the identified invasion-associated regulatory state was supported across multiple complementary levels of analysis, including transcriptomic and epigenomic profiling in a serially selected patient-derived glioblastoma model, validation of invasion-associated methylation patterns in independent patient-derived glioma stem-like cultures, functional perturbation of candidate regulatory networks in additional glioblastoma models, and association of invasion-linked transcriptional and epigenetic signatures with patient outcome in TCGA cohorts. Our findings support a model in which glioblastoma invasion is associated with an epigenetically primed regulatory state that shapes context-specific transcription factor activity and stabilizes invasion-associated gene expression programs. In this framework, invasive capacity is not simply induced by external cues but can emerge through selection of cells with a preconfigured, invasion-primed regulatory landscape. While invasion plasticity remains a defining feature of glioblastoma biology, our data suggest that epigenetically maintained subpopulations may provide a persistent reservoir of invasive potential.

Finally, it should be noted that our model is based on patient-derived *in vitro* systems, which allow controlled investigation of cell-intrinsic regulatory states but do not fully capture the spatial and microenvironmental complexity of glioblastoma *in vivo*. From a clinical perspective, the observed association of invasion-linked methylation and gene expression signatures with patient survival suggests that such regulatory states are reflected in tumor biology and may provide a framework for improved patient stratification. Moreover, these findings highlight epigenetic regulation and transcriptional network reorganization as central features of glioblastoma progression in the context of invasive disease and potential entry points for therapeutic intervention.

Declarations

Ethics approval and consent to participate

The study primarily used established human glioblastoma cell lines and previously established patient-derived glioblastoma stem-like cultures generated under the approvals under which they were originally established. Additional patient-derived glioblastoma samples included in the supplementary analyses were obtained at the University Hospital Frankfurt after written informed consent under approval of the Ethics Committee of the University Hospital Frankfurt (approval number SNO-12-2020). All procedures were performed in accordance with the Declaration of Helsinki where applicable.

Consent for publication

Not applicable.

Competing interests

The authors declare that they have no competing interests.

Funding

T.B. was supported by the Arthur und Margarete Ebert-Stiftung. A.-C.H. was supported by the Mildred Scheel Career Center Frankfurt (Deutsche Krebshilfe) and the WISER Fellowship. J.S. received funding from the Wilhelm Sander-Stiftung. V.L. was supported by the Rosa-Luxemburg Foundation (BMBF) and a Walter Benjamin Fellowship (DFG, LA 5922/1).

Acknowledgements

We thank Nathalie Nicot and Barbara Klink for sequencing support and Michael Ronellenfitsch for providing the LNT-229 ATF4 knockdown and corresponding control cell lines, and Prof. Kavi Devraj for

critical review of the manuscript and insightful scientific discussions.

Author contributions

T.B. and A.-C.H. conceived the study and supervised the project. T.B., S.S., and C.C. performed most of the experimental work and acquired the data. L.F.H. and K.K.C. specifically performed inhibitor studies and associated transwell invasion assays, including experiments using ATF4 knockdown cells. T.K. performed the corresponding flow cytometric analyses. T.B., J.S., and K.K.C. routinely sampled fresh patient tissues for organoid and glioblastoma stem-like cultures. A.-C.H. performed DNA methylation experiments and analyses. A.M., P.N., and V.L. performed the bioinformatic and statistical analyses. T.B. and A.-C.H. wrote the original draft of the manuscript. All authors reviewed and edited the manuscript. K.H.P., J.P.S., and M.M. provided resources, institutional support, and scientific guidance.

Data availability statement

RNA sequencing and DNA methylation data generated in this study have been deposited in the NCBI Gene Expression Omnibus (GEO) under accession numbers GSE324631 (RNA sequencing) and GSE324664 (DNA methylation). Processed datasets required to reproduce the main figures, including normalized expression matrices and differential expression and DNA methylation results, are included in the GEO submission and will become publicly available upon publication. Reviewer access is available upon request. Additional data supporting the findings of this study are available from the corresponding authors upon reasonable request.

References

1. N. A. Khiabani *et al.*, ‘Glioblastoma therapy: State of the field and future prospects’, *Life Sci.*, vol. 359, p. 123227, Dec. 2024, doi: 10.1016/j.lfs.2024.123227.
2. D. Sipos *et al.*, ‘Glioblastoma: Clinical Presentation, Multidisciplinary Management, and Long-Term Outcomes’, *Cancers (Basel).*, vol. 17, no. 1, p. 146, Jan. 2025, doi: 10.3390/cancers17010146.
3. M. J. van den Bent *et al.*, ‘Primary brain tumours in adults’, *The Lancet*, vol. 402, no. 10412, pp. 1564–1579, Oct. 2023, doi: 10.1016/S0140-6736(23)01054-1.
4. M. C. de Gooijer, M. Guillén Navarro, R. Bernards, T. Wurdinger, and O. van Tellingen, ‘An Experimenter’s Guide to Glioblastoma Invasion Pathways’, *Trends Mol. Med.*, vol. 24, no. 9, pp. 763–780, Sep. 2018, doi: 10.1016/j.molmed.2018.07.003.
5. F. Revilla-Pacheco *et al.*, ‘Extent of resection and survival in patients with glioblastoma multiforme’, *Medicine*, vol. 100, no. 25, p. e26432, Jun. 2021, doi: 10.1097/MD.0000000000026432.
6. C. W. Brennan *et al.*, ‘The Somatic Genomic Landscape of Glioblastoma’, *Cell*, vol. 155, no. 2, pp. 462–477, Oct. 2013, doi: 10.1016/j.cell.2013.09.034.

7. M. Nomura *et al.*, ‘The multilayered transcriptional architecture of glioblastoma ecosystems’, *Nat. Genet.*, vol. 57, no. 5, pp. 1155–1167, May 2025, doi: 10.1038/s41588-025-02167-5.
8. C. Neftel *et al.*, ‘An Integrative Model of Cellular States, Plasticity, and Genetics for Glioblastoma’, *Cell*, vol. 178, no. 4, pp. 835-849.e21, Aug. 2019, doi: 10.1016/j.cell.2019.06.024.
9. A. C. Greenwald *et al.*, ‘Integrative spatial analysis reveals a multi-layered organization of glioblastoma’, *Cell*, vol. 187, no. 10, pp. 2485-2501.e26, May 2024, doi: 10.1016/j.cell.2024.03.029.
10. A. P. Patel *et al.*, ‘Single-cell RNA-seq highlights intratumoral heterogeneity in primary glioblastoma’, *Science (1979).*, vol. 344, no. 6190, pp. 1396–1401, Jun. 2014, doi: 10.1126/science.1254257.
11. P. Friedl and S. Alexander, ‘Cancer Invasion and the Microenvironment: Plasticity and Reciprocity’, *Cell*, vol. 147, no. 5, pp. 992–1009, Nov. 2011, doi: 10.1016/j.cell.2011.11.016.
12. A. Vollmann-Zwerenz, V. Leidgens, G. Feliciello, C. A. Klein, and P. Hau, ‘Tumor Cell Invasion in Glioblastoma’, *Int. J. Mol. Sci.*, vol. 21, no. 6, p. 1932, Mar. 2020, doi: 10.3390/ijms21061932.
13. I. Koh, J. Cha, J. Park, J. Choi, S.-G. Kang, and P. Kim, ‘The mode and dynamics of glioblastoma cell invasion into a decellularized tissue-derived extracellular matrix-based three-dimensional tumor model’, *Sci. Rep.*, vol. 8, no. 1, p. 4608, Mar. 2018, doi: 10.1038/s41598-018-22681-3.
14. D. B. Mair, H. M. Ames, and R. Li, ‘Mechanisms of invasion and motility of high-grade gliomas in the brain’, *Mol. Biol. Cell*, vol. 29, no. 21, pp. 2509–2515, Oct. 2018, doi: 10.1091/mbc.E18-02-0123.
15. A. Dirkse *et al.*, ‘Stem cell-associated heterogeneity in Glioblastoma results from intrinsic tumor plasticity shaped by the microenvironment’, *Nat. Commun.*, vol. 10, no. 1, p. 1787, Apr. 2019, doi: 10.1038/s41467-019-09853-z.
16. A. Fayzullin *et al.*, ‘Phenotypic and Expressional Heterogeneity in the Invasive Glioma Cells’, *Transl. Oncol.*, vol. 12, no. 1, pp. 122–133, Jan. 2019, doi: 10.1016/j.tranon.2018.09.014.
17. R. Rezk *et al.*, ‘Spatial heterogeneity of cell-matrix adhesive forces predicts human glioblastoma migration’, *Neurooncol. Adv.*, vol. 2, no. 1, Jan. 2020, doi: 10.1093/noajnl/vdaa081.
18. Y. A. Yabo, S. P. Niclou, and A. Golebiewska, ‘Cancer cell heterogeneity and plasticity: A paradigm shift in glioblastoma’, *Neuro. Oncol.*, vol. 24, no. 5, pp. 669–682, May 2022, doi: 10.1093/neuonc/noab269.
19. M. Doroszko *et al.*, ‘The invasion phenotypes of glioblastoma depend on plastic and reprogrammable cell states’, *Nat. Commun.*, vol. 16, no. 1, p. 6662, Jul. 2025, doi: 10.1038/s41467-025-61999-1.
20. A. Schuster *et al.*, ‘AN1-type zinc finger protein 3 (ZFAND3) is a transcriptional regulator that drives Glioblastoma invasion’, *Nat. Commun.*, vol. 11, no. 1, p. 6366, Dec. 2020, doi: 10.1038/s41467-020-20029-y.
21. Y. Xiao *et al.*, ‘Ex vivo Dynamics of Human Glioblastoma Cells in a Microvasculature-on-a-Chip System Correlates with Tumor Heterogeneity and Subtypes’, *Advanced Science*, vol. 6, no. 8, Apr. 2019, doi: 10.1002/advs.201801531.
22. A. Fayzullin *et al.*, ‘Time-lapse phenotyping of invasive glioma cells ex vivo reveals subtype-specific movement patterns guided by tumor core signaling’, *Exp. Cell Res.*, vol. 349, no. 2, pp. 199–213, Dec. 2016, doi: 10.1016/j.yexcr.2016.08.001.

23. C. Garcia-Diaz *et al.*, 'Glioblastoma cell fate is differentially regulated by the microenvironments of the tumor bulk and infiltrative margin', *Cell Rep.*, vol. 42, no. 5, p. 112472, May 2023, doi: 10.1016/j.celrep.2023.112472.
24. A. Golebiewska *et al.*, 'Patient-derived organoids and orthotopic xenografts of primary and recurrent gliomas represent relevant patient avatars for precision oncology', *Acta Neuropathol.*, vol. 140, no. 6, pp. 919–949, Dec. 2020, doi: 10.1007/s00401-020-02226-7.
25. S. Marino *et al.*, 'The Extracellular Matrix in Glioblastomas: A Glance at Its Structural Modifications in Shaping the Tumoral Microenvironment—A Systematic Review', *Cancers (Basel).*, vol. 15, no. 6, p. 1879, Mar. 2023, doi: 10.3390/cancers15061879.
26. R. Wei *et al.*, 'VCAN in the extracellular matrix drives glioma recurrence by enhancing cell proliferation and migration', *Front. Neurosci.*, vol. 18, Nov. 2024, doi: 10.3389/fnins.2024.1501906.
27. V. Venkataramani *et al.*, 'Glutamatergic synaptic input to glioma cells drives brain tumour progression', *Nature*, vol. 573, no. 7775, pp. 532–538, Sep. 2019, doi: 10.1038/s41586-019-1564-x.
28. A. Bhaduri *et al.*, 'Outer Radial Glia-like Cancer Stem Cells Contribute to Heterogeneity of Glioblastoma', *Cell Stem Cell*, vol. 26, no. 1, pp. 48-63.e6, Jan. 2020, doi: 10.1016/j.stem.2019.11.015.
29. D. F. Quail and J. A. Joyce, 'The Microenvironmental Landscape of Brain Tumors', *Cancer Cell*, vol. 31, no. 3, pp. 326–341, Mar. 2017, doi: 10.1016/j.ccell.2017.02.009.
30. D. Hambardzumyan, D. H. Gutmann, and H. Kettenmann, 'The role of microglia and macrophages in glioma maintenance and progression', *Nat. Neurosci.*, vol. 19, no. 1, pp. 20–27, Jan. 2016, doi: 10.1038/nn.4185.
31. M. Dapash, D. Hou, B. Castro, C. Lee-Chang, and M. S. Lesniak, 'The Interplay between Glioblastoma and Its Microenvironment', *Cells*, vol. 10, no. 9, p. 2257, Aug. 2021, doi: 10.3390/cells10092257.
32. P. Sharma, A. Aaroe, J. Liang, and V. K. Puduvalli, 'Tumor microenvironment in glioblastoma: Current and emerging concepts', *Neurooncol. Adv.*, vol. 5, no. 1, Jan. 2023, doi: 10.1093/noajnl/vdad009.
33. V. T. Manoharan *et al.*, 'Spatiotemporal modeling reveals high-resolution invasion states in glioblastoma', *Genome Biol.*, vol. 25, no. 1, p. 264, Oct. 2024, doi: 10.1186/s13059-024-03407-3.
34. A. De *et al.*, 'Single cell spatial profiling of the matrisome identifies region-specific adhesion and signaling networks in glioblastoma', *Commun. Biol.*, vol. 9, no. 1, p. 17, Dec. 2025, doi: 10.1038/s42003-025-09270-7.
35. B. Pai *et al.*, 'Spatial Multiomics Defines a Shared Tumor Infiltrative Signature at the Resection Margin in High-Grade Gliomas', *Cancer Res.*, vol. 85, no. 21, pp. 4233–4250, Nov. 2025, doi: 10.1158/0008-5472.CAN-24-4708.
36. P. A. Jones, H. Ohtani, A. Chakravarthy, and D. D. De Carvalho, 'Epigenetic therapy in immune-oncology', *Nat. Rev. Cancer*, vol. 19, no. 3, pp. 151–161, Mar. 2019, doi: 10.1038/s41568-019-0109-9.
37. D. Schübeler, 'Function and information content of DNA methylation', *Nature*, vol. 517, no. 7534, pp. 321–326, Jan. 2015, doi: 10.1038/nature14192.
38. X. Deng, D. Wu, Y. Zhao, Y. Qing, H. Wu, and J. Chen, 'Epitranscriptomic control of cancer hallmarks: Functions, mechanisms, and therapeutics of RNA modifications', *Cancer Cell*, vol. 44, no. 1, pp. 50–

76, Jan. 2026, doi: 10.1016/j.ccell.2025.12.001.

39. J. Yang *et al.*, 'Enhancer reprogramming: critical roles in cancer and promising therapeutic strategies', *Cell Death Discov.*, vol. 11, no. 1, p. 84, Mar. 2025, doi: 10.1038/s41420-025-02366-3.
40. X. Luo and Q. Zou, 'Identifying the "stripe" transcription factors and cooperative binding related to DNA methylation', *Commun. Biol.*, vol. 7, no. 1, p. 1265, Oct. 2024, doi: 10.1038/s42003-024-06992-y.
41. H. Zhu, G. Wang, and J. Qian, 'Transcription factors as readers and effectors of DNA methylation', *Nat. Rev. Genet.*, vol. 17, no. 9, pp. 551–565, Sep. 2016, doi: 10.1038/nrg.2016.83.
42. M. Rimoldi *et al.*, 'DNA methylation patterns of transcription factor binding regions characterize their functional and evolutionary contexts', *Genome Biol.*, vol. 25, no. 1, p. 146, Jun. 2024, doi: 10.1186/s13059-024-03218-6.
43. Y. Yin *et al.*, 'Impact of cytosine methylation on DNA binding specificities of human transcription factors', *Science (1979).*, vol. 356, no. 6337, May 2017, doi: 10.1126/science.aaj2239.
44. É. Héberlé and A. F. Bardet, 'Sensitivity of transcription factors to DNA methylation', *Essays Biochem.*, vol. 63, no. 6, pp. 727–741, Dec. 2019, doi: 10.1042/EBC20190033.
45. S. Koo, G. S. Martin, K. J. Schulz, M. Ronck, and L. G. Toussaint, 'Serial selection for invasiveness increases expression of miR-143/miR-145 in glioblastoma cell lines', *BMC Cancer*, vol. 12, no. 1, p. 143, Dec. 2012, doi: 10.1186/1471-2407-12-143.
46. D. Capper *et al.*, 'DNA methylation-based classification of central nervous system tumours', *Nature*, vol. 555, no. 7697, pp. 469–474, Mar. 2018, doi: 10.1038/nature26000.
47. M. Parlani, C. Jorgez, and P. Friedl, 'Plasticity of cancer invasion and energy metabolism', *Trends Cell Biol.*, vol. 33, no. 5, pp. 388–402, May 2023, doi: 10.1016/j.tcb.2022.09.009.
48. K. E. de Visser and J. A. Joyce, 'The evolving tumor microenvironment: From cancer initiation to metastatic outgrowth', *Cancer Cell*, vol. 41, no. 3, pp. 374–403, Mar. 2023, doi: 10.1016/j.ccell.2023.02.016.
49. Y. Zhang *et al.*, 'Mechanical forces in the tumor microenvironment: roles, pathways, and therapeutic approaches', *J. Transl. Med.*, vol. 23, no. 1, p. 313, Mar. 2025, doi: 10.1186/s12967-025-06306-8.
50. Y. Xiao *et al.*, 'Ex vivo Dynamics of Human Glioblastoma Cells in a Microvasculature-on-a-Chip System Correlates with Tumor Heterogeneity and Subtypes', *Advanced Science*, vol. 6, no. 8, Apr. 2019, doi: 10.1002/advs.201801531.
51. I. Manini *et al.*, 'Role of Microenvironment in Glioma Invasion: What We Learned from In Vitro Models', *Int. J. Mol. Sci.*, vol. 19, no. 1, p. 147, Jan. 2018, doi: 10.3390/ijms19010147.
52. L. R. Decotret, R. Shi, K. N. Thomas, M. Hsu, C. J. Pallen, and K. L. Bennewith, 'Development and validation of an advanced ex vivo brain slice invasion assay to model glioblastoma cell invasion into the complex brain microenvironment', *Front. Oncol.*, vol. 13, Jan. 2023, doi: 10.3389/fonc.2023.976945.
53. V. V. Artym, K. Matsumoto, S. C. Mueller, and K. M. Yamada, 'Dynamic membrane remodeling at invadopodia differentiates invadopodia from podosomes', *Eur. J. Cell Biol.*, vol. 90, no. 2–3, pp. 172–180, Feb. 2011, doi: 10.1016/j.ejcb.2010.06.006.

54. F. B. Furnari *et al.*, ‘Malignant astrocytic glioma: genetics, biology, and paths to treatment’, *Genes Dev.*, vol. 21, no. 21, pp. 2683–2710, Nov. 2007, doi: 10.1101/gad.1596707.
55. V. M. Ravi *et al.*, ‘Spatially resolved multi-omics deciphers bidirectional tumor-host interdependence in glioblastoma’, *Cancer Cell*, vol. 40, no. 6, pp. 639-655.e13, Jun. 2022, doi: 10.1016/j.ccell.2022.05.009.
56. S. C. Mack *et al.*, ‘Chromatin landscapes reveal developmentally encoded transcriptional states that define human glioblastoma’, *Journal of Experimental Medicine*, vol. 216, no. 5, pp. 1071–1090, May 2019, doi: 10.1084/jem.20190196.
57. S. Kaluscha *et al.*, ‘Evidence that direct inhibition of transcription factor binding is the prevailing mode of gene and repeat repression by DNA methylation’, *Nat. Genet.*, vol. 54, no. 12, pp. 1895–1906, Dec. 2022, doi: 10.1038/s41588-022-01241-6.
58. L. Isbel, R. S. Grand, and D. Schübeler, ‘Generating specificity in genome regulation through transcription factor sensitivity to chromatin’, *Nat. Rev. Genet.*, vol. 23, no. 12, pp. 728–740, Dec. 2022, doi: 10.1038/s41576-022-00512-6.
59. Y. Yin *et al.*, ‘Impact of cytosine methylation on DNA binding specificities of human transcription factors’, *Science (1979).*, vol. 356, no. 6337, May 2017, doi: 10.1126/science.aaj2239.
60. M. V. C. Greenberg and D. Bourc’his, ‘The diverse roles of DNA methylation in mammalian development and disease’, *Nat. Rev. Mol. Cell Biol.*, vol. 20, no. 10, pp. 590–607, Oct. 2019, doi: 10.1038/s41580-019-0159-6.
61. M. R. Corces *et al.*, ‘The chromatin accessibility landscape of primary human cancers’, *Science (1979).*, vol. 362, no. 6413, Oct. 2018, doi: 10.1126/science.aav1898.
62. M. Vita and M. Henriksson, ‘The Myc oncoprotein as a therapeutic target for human cancer’, *Semin. Cancer Biol.*, vol. 16, no. 4, pp. 318–330, Aug. 2006, doi: 10.1016/j.semcancer.2006.07.015.
63. O. Zaytseva, N. Kim, and L. M. Quinn, ‘MYC in Brain Development and Cancer’, *Int. J. Mol. Sci.*, vol. 21, no. 20, p. 7742, Oct. 2020, doi: 10.3390/ijms21207742.
64. B. Lan *et al.*, ‘Triggering of endoplasmic reticulum stress via ATF4-SPHK1 signaling promotes glioblastoma invasion and chemoresistance’, *Cell Death Dis.*, vol. 15, no. 8, p. 552, Aug. 2024, doi: 10.1038/s41419-024-06936-8.

Figures

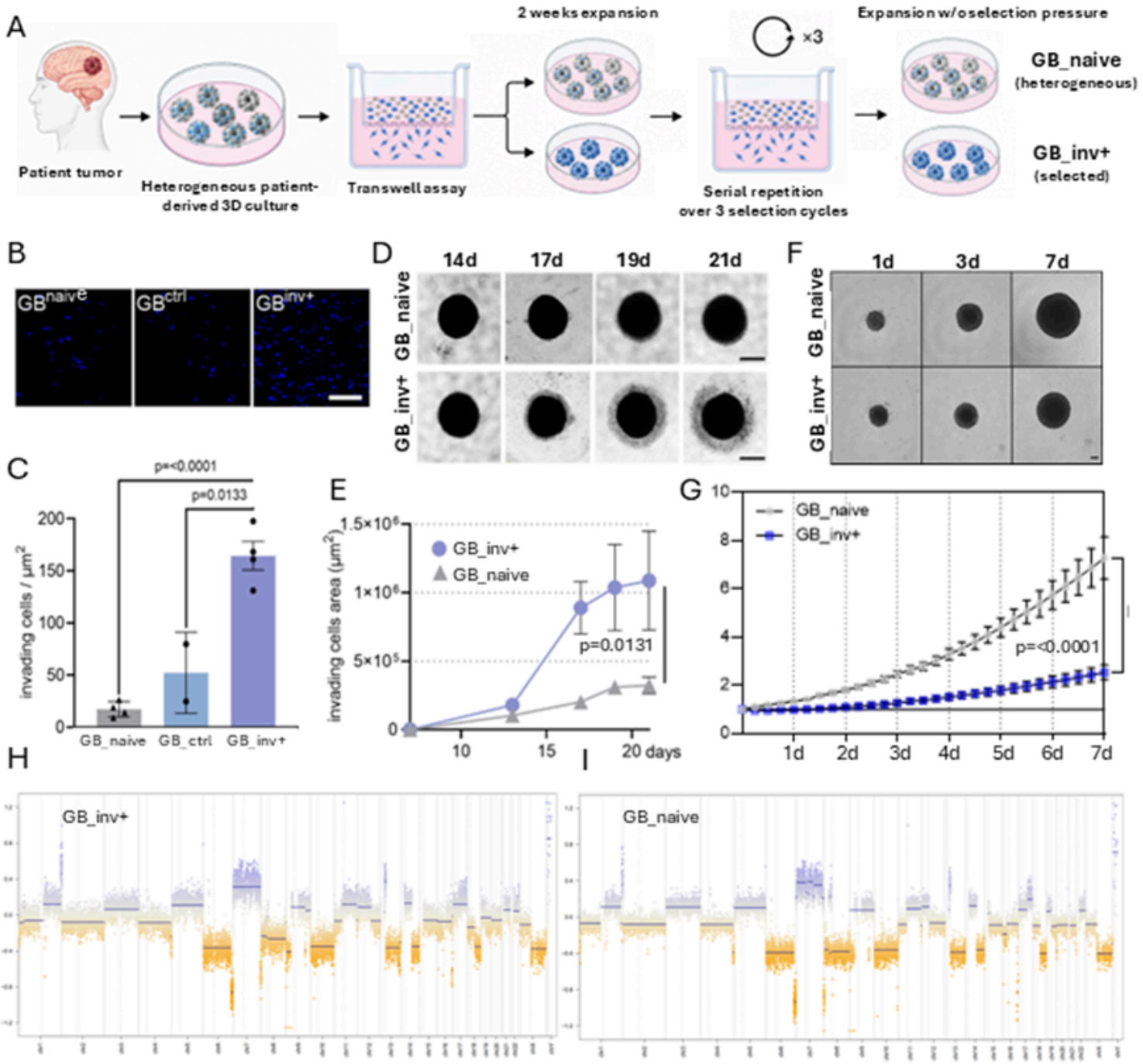

Figure 1

Serial selection of invasive glioblastoma cells generates an isogenic subpopulation with enhanced invasive capacity. (A) Schematic overview of the serial selection workflow used to enrich for invasive glioblastoma cells. Patient-derived GB cells were maintained under serum-free conditions and subjected to repeated transwell invasion followed by re-expansion over three selection rounds (>2 weeks per round), enriching for a highly invasive subpopulation termed GB_inv+. In parallel, the heterogeneous parental population (GB_naive) was expanded under identical culture conditions without transwell selection. (B) Representative fluorescence images of transwell invasion assays showing DAPI-stained invading cells of

GB_naive, GB_ctrl and GB_inv+ cultures after 24 h (10× objective; scale bar = 50 µm). (C) Quantification of invading cells in the transwell invasion assay. Invading nuclei were quantified from fluorescence images and expressed as invading cells per µm² (n = 4 biological replicates). Data are shown as mean ± SEM. Statistical analysis: unpaired two-tailed Student's t-test. (D) Representative brightfield images of spheroid invasion assays acquired after 14, 17, 19 and 21 days following embedding in Matrigel (10× objective; scale bar = 500 µm). (E) Quantification of spheroid invasion. The invaded cell area surrounding the spheroid was measured over time and was significantly increased in GB_inv+ compared with GB_naive spheroids (n = 4 biological replicates). Data are shown as mean ± SEM. Statistical analysis: unpaired two-tailed Student's t-test. (F) Representative brightfield images of 3D spheroid proliferation assays at days 1, 3 and 7 (scale bar = 100 µm). (G) Quantification of spheroid growth over seven days. Spheroid area is shown as fold change relative to day 0 (n = 3 biological replicates). Data are presented as mean ± SEM. Statistical analysis: unpaired two-tailed Student's t-test. (H, I) Representative genome-wide copy number variation (CNV) profiles inferred from DNA methylation array data of GB_inv+ (H) and GB_naive (I) cells. Highly similar CNV patterns indicate preservation of the genomic background following serial invasion selection.

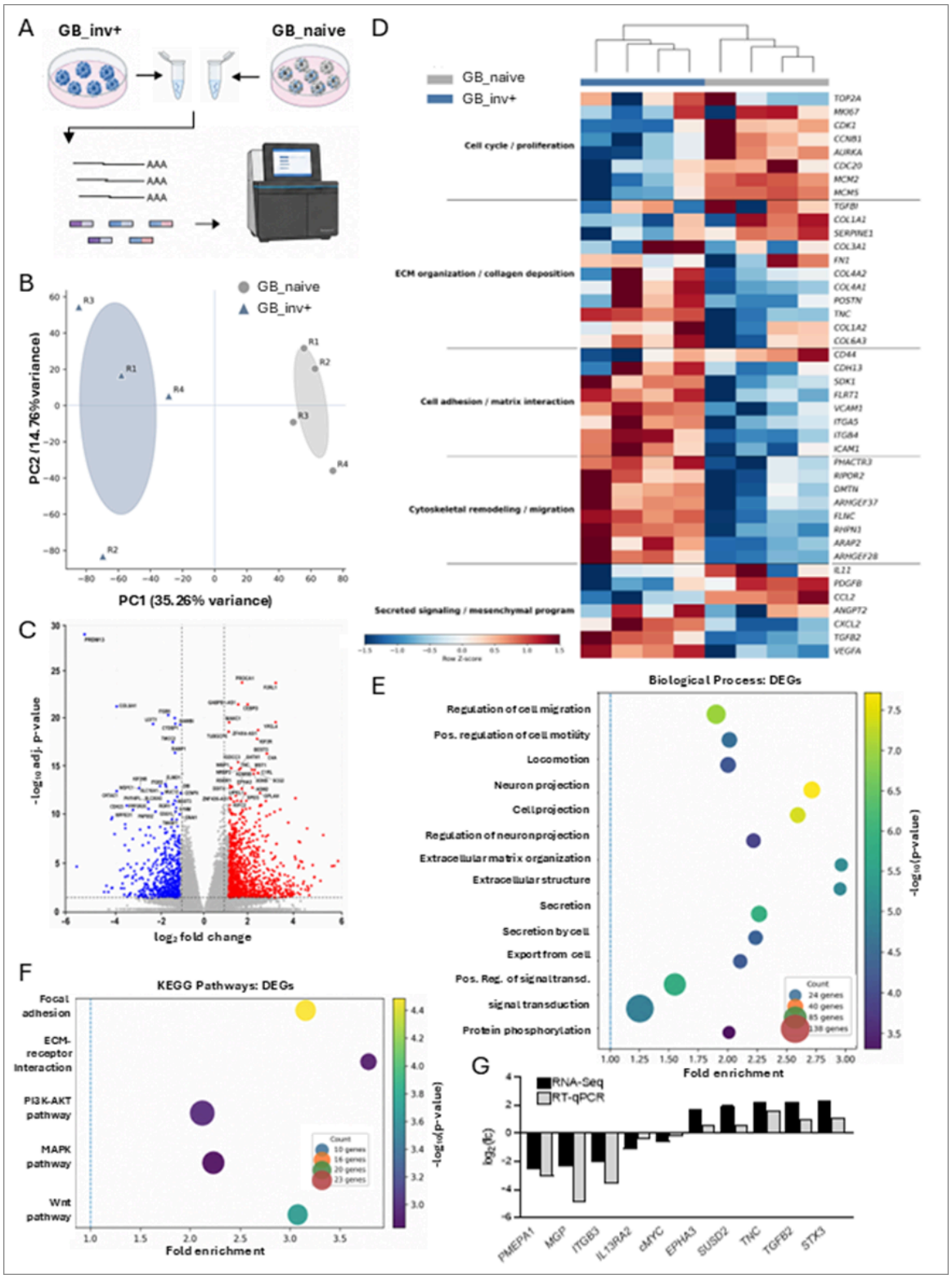

Figure 2

Transcriptomic profiling reveals an invasion-associated gene expression program in GB_inv+ cells. (A) Schematic overview of the RNA sequencing workflow. Total RNA was isolated from GB_naive and GB_inv+ cells (n = 4 biological replicates per group) and subjected to bulk RNA sequencing followed by differential gene expression and pathway analyses. (B) Principal component analysis (PCA) of RNA-seq data demonstrates clear segregation of GB_naive and GB_inv+ samples, indicating distinct transcriptional

programs associated with the invasion-selected phenotype. (C) Volcano plot of differentially expressed genes between GB_inv+ and GB_naive cells. Red and blue dots indicate significantly up- and downregulated genes, respectively ($|\log_2$ fold change$| \geq 1.2$, adjusted $P < 0.05$). (D) Heatmap of representative differentially expressed genes grouped according to their biological function. GB_inv+ cells display reduced expression of cell cycle- and proliferation-associated genes and increased expression of genes involved in extracellular matrix organization, cell adhesion, cytoskeletal remodeling, migration and mesenchymal signaling. (E) Gene Ontology (Biological Process) enrichment analysis of differentially expressed genes identifies significant enrichment of pathways related to cell migration, cell motility, extracellular matrix organization, cell projection, secretion and signaling. (F) KEGG pathway enrichment analysis highlights focal adhesion, ECM-receptor interaction, PI3K-AKT, MAPK and WNT signaling as major pathways associated with the invasion-selected phenotype. (G) RT-qPCR validation of selected differentially expressed genes confirms the RNA-seq findings. Gene expression changes are shown as $\log_2$ fold change relative to GB_naive cells.

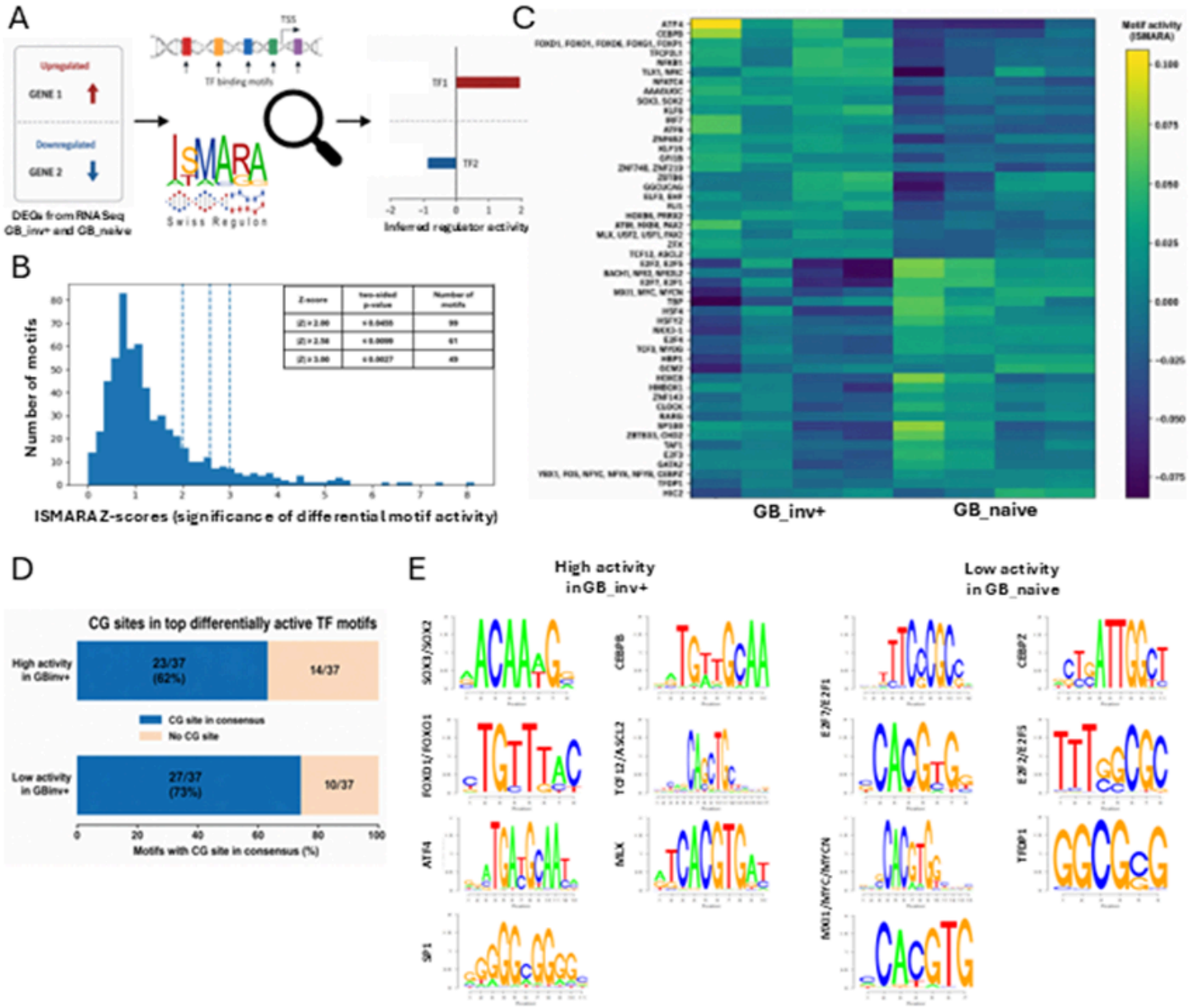

Figure 3

Regulatory network analysis identifies transcription factor programs associated with the invasion-selected phenotype. (A) Schematic overview of the ISMARA analysis workflow. RNA-seq data from GB_naive and GB_inv+ samples were uploaded to the ISMARA platform, which automatically inferred transcription factor motif activities from genome-wide expression profiles by integrating promoter sequence information and predict transcription factor binding motifs. (B) Distribution of ISMARA-derived motif activity Z-scores across all analyzed transcription factor motifs between GB_inv+ and GB_naive samples. Dashed lines indicate significance thresholds (|Z| ≥ 2.0, 2.58 and 3.0). The box summarizes the number of significantly differentially active motifs identified at each threshold. (C) Heatmap of the top differentially active transcription factor motifs across GB_inv+ and GB_naive samples. Rows represent

inferred TF motif activities and columns represent biological replicates (n = 4). Color intensity indicates relative motif activity inferred by ISMARA. (D) Frequency of CpG dinucleotides within the consensus sequences of the top differentially active transcription factor motifs. Most motifs with increased activity in GB_inv+ (23/37, 62%) and decreased activity in GB_inv+ (27/37, 73%) contain at least one CpG dinucleotide within their consensus sequence. (E) Representative sequence logos of transcription factor binding motifs with increased activity in GB_inv+ (left) and decreased activity in GB_inv+ (right). Increased motif activity in GB_inv+ was observed for regulators associated with stress response, metabolic regulation and adaptive transcriptional programs (e.g., ATF4, CEBPB, MLX), whereas motifs associated with proliferative programs (e.g., E2F family and MYC/MYCN-related motifs) displayed reduced activity.

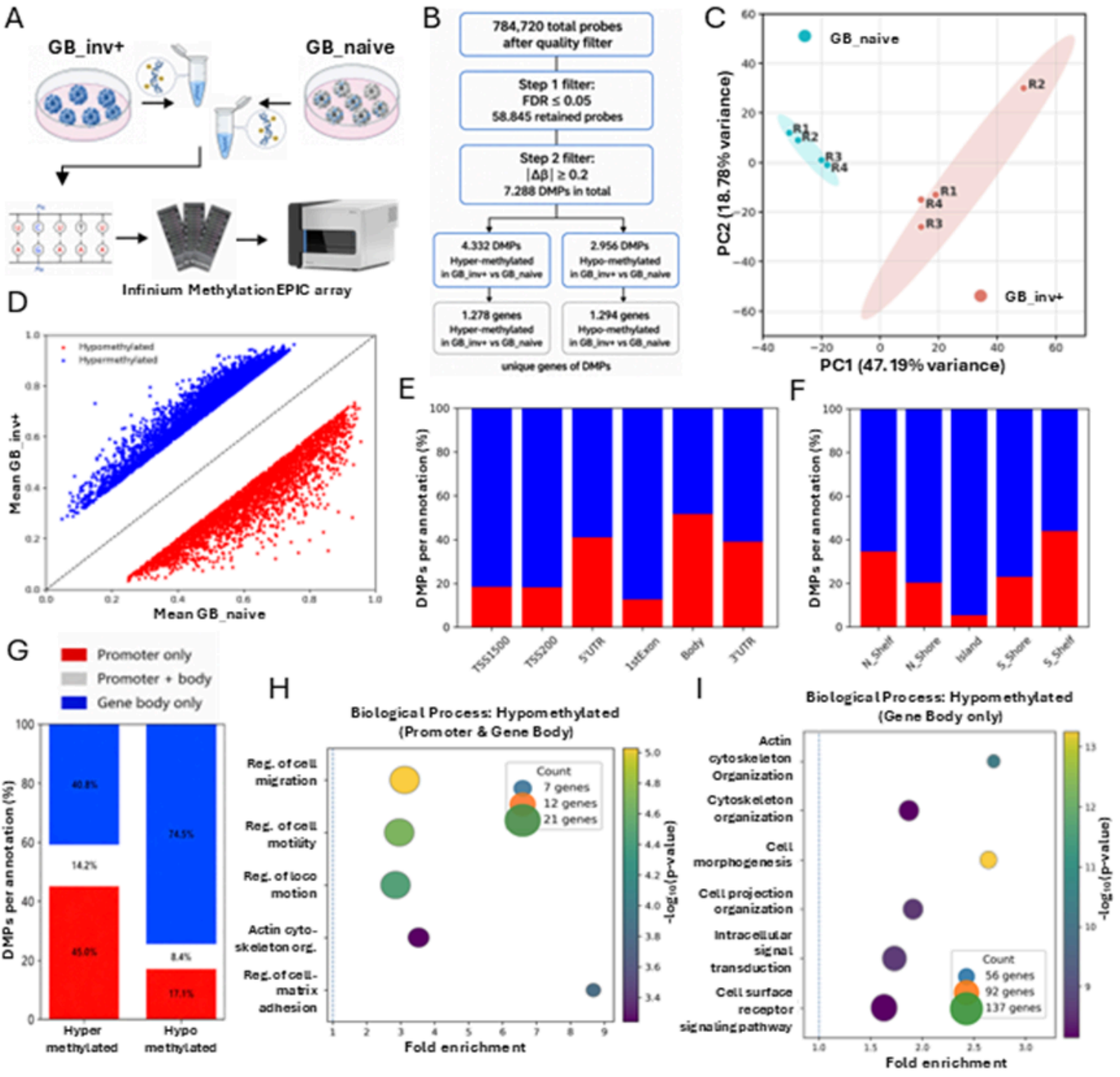

Figure 4

Genome-wide DNA methylation profiling identifies an invasion-associated epigenetic landscape in GB_inv+ cells. (A) Schematic overview of the DNA methylation workflow. Genomic DNA isolated from GB_naive and GB_inv+ cells (n = 4 biological replicates per group) was analyzed using the Infinium MethylationEPIC BeadChip array to identify differentially methylated probes (DMPs) between both conditions. (B) Filtering strategy for identification of DMPs. After quality filtering, 784,720 probes were retained. Step 1 filtering (FDR < 0.05) yielded 58,845 probes, followed by Step 2 filtering ($|\Delta\beta| \geq 0.2$), resulting in 7,288 significantly DMPs. Of these, 4,332 were hypermethylated and 2,956 hypomethylated in GB_inv+ compared to GB_naive, corresponding to 1,278 hypermethylated and 1,294 hypomethylated unique genes. (C) PCA of methylation profiles showing separation between GB_inv+ and GB_naive samples. PC1 and PC2 explain 47.19% and 18.78% of the variance, respectively. (D) Scatter plot comparing mean methylation levels (β-values) between GB_inv+ and GB_naive samples. Each dot represents a probe. Hypermethylated probes (blue) and hypomethylated probes (red) are defined based on $|\Delta\beta| \geq 0.2$. The dashed line indicates equal methylation between conditions. (E) Distribution of DMPs across genomic features (TSS1500, TSS200, 5'UTR, 1st exon, gene body, 3'UTR) and (F) CpG island context (N_shelf, N_shore, island, S_shore, S_shelf). (G) Overall distribution of hypermethylated and hypomethylated DMPs according to genomic location, illustrating the preferential localization of hypermethylated probes to promoter-associated regions and hypomethylated probes within gene bodies. (H) Gene Ontology (Biological Process) enrichment analysis of genes associated with promoter and gene body hypomethylated DMPs identifies enrichment of biological processes related to regulation of cell migration, cell motility, locomotion, actin cytoskeleton organization and cell-matrix adhesion. (I) Gene Ontology (Biological Process) enrichment analysis of genes associated with gene body only hypomethylated DMPs identifies enrichment of pathways associated with cytoskeleton organization, cell morphogenesis, cell projection organization, intracellular signal transduction and cell surface receptor signaling.

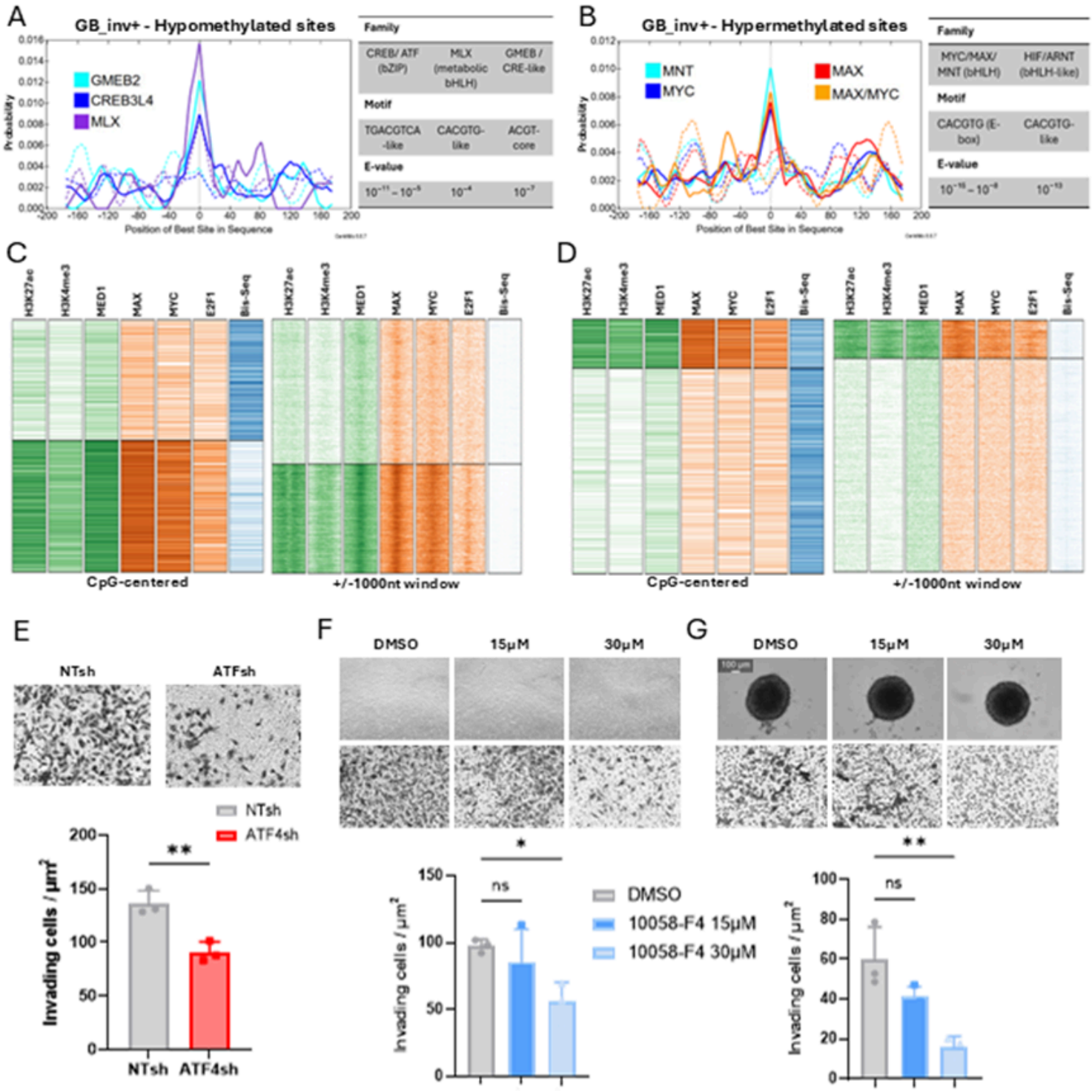

Figure 5

Transcription factor motif enrichment, chromatin context and functional validation of MYC/MAX signaling in invasive glioblastoma. (A) CentriMo analysis of hypomethylated CpG sites in GB_inv+ versus GB_naive cells reveals significant enrichment of motifs associated with CREB/ATF family transcription factors (including CREB3L4 and GMEB2), as well as MLX-related bHLH factors. Probability plots demonstrate preferential localization of transcription factor binding motifs at the center of hypomethylated regions. The accompanying summary highlights representative TF families, consensus

motifs, and corresponding E-values. (B) CentriMo analysis of hypermethylated CpG sites identifies strong enrichment of E-box–containing motifs (CACGTG), associated with the MYC/MAX/MNT transcriptional network, as well as HIF/ARNT-related motifs. (C) Heatmaps showing ChIP-seq signal intensity of histone modifications (H3K27ac, H3K4me3), mediator complex subunit MED1, and transcription factors (MAX, MYC, E2F1) at genomic regions corresponding to differentially methylated CpG sites, using publicly available datasets from U87 glioblastoma cells. For hypomethylated CpG sites, signal is shown centered on the CpG position (left) and across a ±1000 bp window (right). Hypomethylated regions display strong enrichment of active chromatin marks and TF binding in both representations. Public bisulfite-sequencing data are shown at CpG-centered resolution. (D) Heatmaps for hypermethylated CpG sites displayed using the same layout as in (C), with CpG-centered signal on the left and ±1000 bp window on the right. Regions corresponding to hypermethylated CpGs show reduced chromatin activity and reduced TF occupancy compared to hypomethylated regions. (E) Functional validation of the CREB/ATF pathway. Representative transwell invasion images and quantification demonstrate significantly reduced invasion following shRNA-mediated ATF4 knockdown compared with non-targeting control shRNA (NTsh). (F) Pharmacological inhibition of MYC/MAX dimerization using 10058-F4 in adherent LN229 cells. Representative brightfield images of cell cultures following treatment with DMSO, 15 μM or 30 μM 10058-F4 (top), representative transwell invasion images (middle), and quantification of invading cells (bottom) demonstrate a concentration-dependent reduction in invasion (n = 3 biological replicates, scale bar = 750 μm). (G) Pharmacological inhibition of MYC/MAX dimerization in patient-derived glioma stem like cells (GSCs). Representative brightfield images of spheroids following treatment with DMSO, 15 μM or 30 μM 10058-F4 (top), representative transwell invasion images (middle), and quantification of invading cells (bottom) demonstrate a dose-dependent reduction in invasive capacity (n = 3 biological replicates, scale bar = 100 μm).

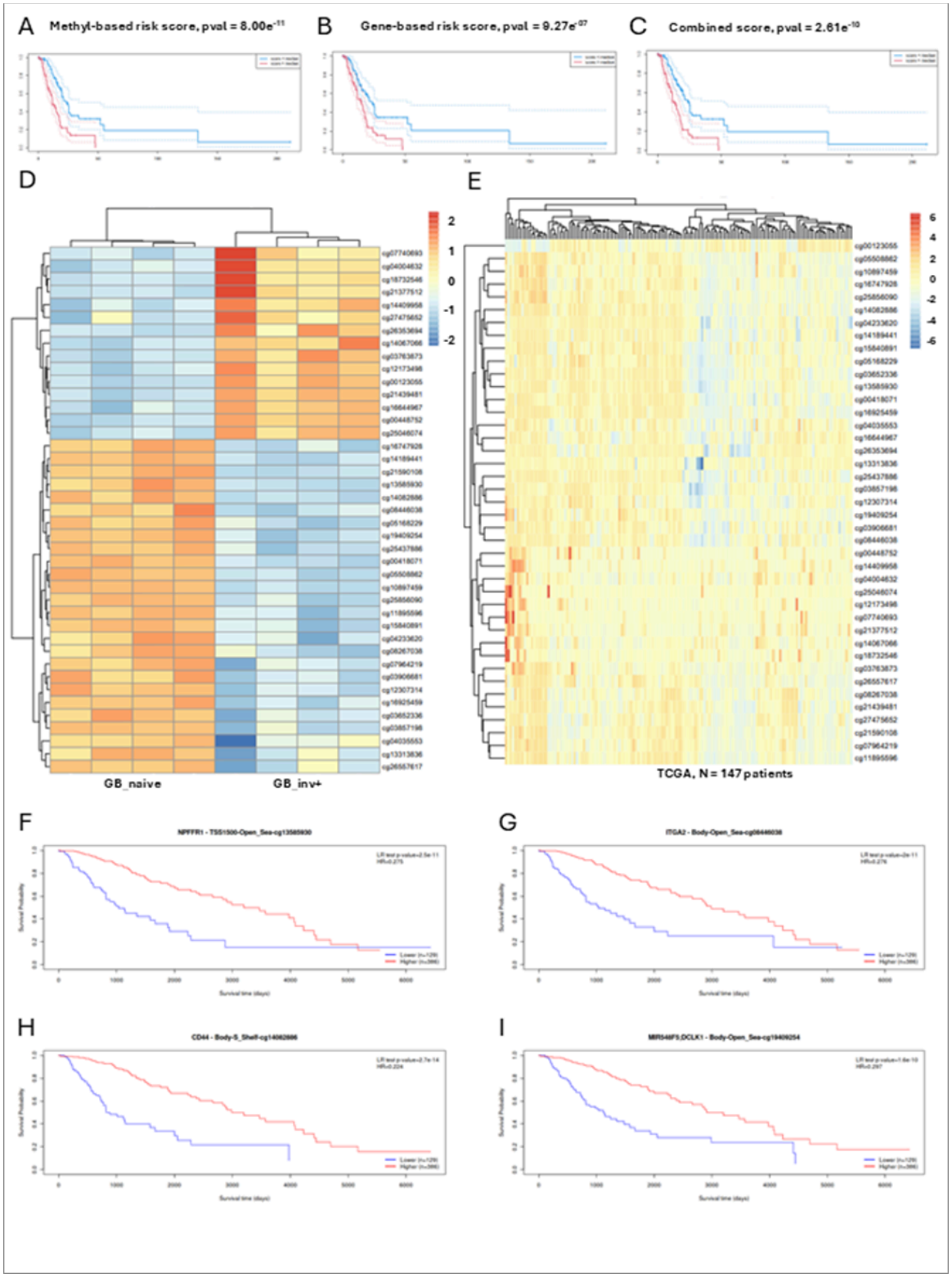

Figure 6

Clinical relevance of invasion-associated methylation and gene expression signatures in glioblastoma. (A) Kaplan–Meier survival analysis of TCGA IDH-wildtype glioblastoma patients stratified by a methylation-based risk score derived from invasion-associated CpG sites. Patients were dichotomized based on the median score. (B) Kaplan–Meier survival analysis based on a gene expression-derived risk score calculated from invasion-associated differentially expressed genes. (C) Combined risk score

integrating methylation and gene expression features, showing robust stratification of patient survival. (D) Heatmap of invasion-associated CpG methylation patterns distinguishing naive and invasive glioblastoma cell populations. (E) Heatmap of prognostic invasion-associated CpG sites significantly associated with overall survival in the TCGA IDH-wildtype glioblastoma cohort (Cox proportional hazards analysis, FDR < 0.05; n = 147). (F-I) Representative Kaplan–Meier survival analyses for selected hypomethylated CpG sites from the invasion-associated methylation signature, (F) NPFFR1, (G) ITGA2, (H) CD44, and (I) DCLK1 (MIR548F5/DCLK1 locus), illustrating the association between lower methylation levels and reduced overall survival in GBM patients.